

# Mechanistic Insight into the Antibacterial Activity of Chitosan Exfoliated MoS<sub>2</sub> Nanosheets: Membrane Damage, Metabolic Inactivation, and Oxidative Stress

Shounak Roy,<sup>†</sup> Anupam Mondal,<sup>†</sup> Varnika Yadav,<sup>†</sup> Ankita Sarkar,<sup>†</sup> Ruptanu Banerjee,<sup>†</sup><sup>ID</sup> Pallab Sanpui,<sup>\*,†</sup><sup>ID</sup> and Amit Jaiswal<sup>\*,†</sup><sup>ID</sup>

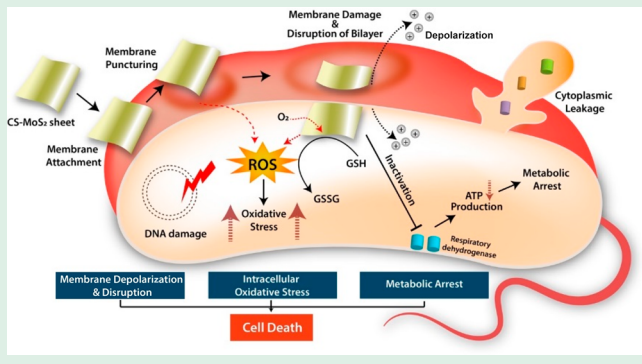
<sup>†</sup>School of Basic Sciences, Indian Institute of Technology Mandi, Kamand, Mandi, Himachal Pradesh 175005, India

<sup>\*</sup>Department of Biotechnology, BITS Pilani, Dubai Campus, PO Box 345055, Dubai International Academic City, Dubai, United Arab Emirates

## Supporting Information

**ABSTRACT:** Two-dimensional molybdenum disulfide (MoS<sub>2</sub>) based nanosheets functionalized or loaded with an antimicrobial agent have recently attracted attention as highly efficient antibacterial agent. MoS<sub>2</sub> sheets act as the photothermal transducers in inducing bacterial cell death on impingement of NIR radiation or enabled cell inactivation by wrapping around the cells. However, the intrinsic ability of MoS<sub>2</sub> to act as an effective antibacterial agent without the use of any external stimuli or antimicrobial agent is still not well explored. This study provides a detailed mechanism of antibacterial action of chitosan exfoliated MoS<sub>2</sub> nanosheets (CS-MoS<sub>2</sub>) by deciphering the key events happening both at the membrane surface and inside the bacteria as a result of interaction of bacterial cells with the nanosheets. A simple, green, one-step process was employed for synthesizing stable and positively charged MoS<sub>2</sub> nanosheets. The prepared nanosheets showed excellent bactericidal activity against both Gram-positive (MIC = 90 µg/mL, MBC = 120 µg/mL) and Gram-negative bacteria (MIC = 30 µg/mL, MBC = 60 µg/mL). Investigations into deciphering the mechanism of action revealed that the CS-MoS<sub>2</sub> nanosheets interacted strongly with the bacterial cells through electrostatic interactions and caused rapid depolarization of the membranes through dent formations. On account of strong van der Waals and electrostatic forces occurring between the CS-MoS<sub>2</sub> nanosheets and membrane phospholipid molecules, deepening of dents occurred, which resulted in complete membrane disruption and leakage of cytoplasmic contents. This led to inactivation of the bacterial respiratory pathway through inhibition of dehydrogenase enzymes and induced metabolic arrest in the cells. Simultaneously, disruption of the antioxidant defense system of the cells by increased levels of intracellular ROS subjected the cells to oxidative damage and added to the overall bactericidal action. The nanosheets also displayed antibiofilm properties and were found to be compatible with mammalian cells even at high concentrations.

**KEYWORDS:** MoS<sub>2</sub> nanosheet, chitosan, antibacterial, membrane damage, metabolic inactivation, oxidative stress, antibiofilm



## 1. INTRODUCTION

The widespread emergence of microbial resistance to the existing line of antibiotics has turned out to be a global health concern.<sup>1</sup> This has led to the search for alternate antimicrobial agents that can selectively and efficiently kill the pathogenic strains without causing any adverse side-effects to the host.<sup>2</sup> Nanomaterials have emerged as a novel class of antibacterial agents that have shown high bactericidal efficiency against drug resistant strains without inducing generation of resistance and are currently being considered as an important alternative therapeutic agent for controlling the problem of drug resistance.<sup>3,4</sup> Among the class of nanomaterials, silver nanoparticles have been most extensively studied and exploited as antibacterial agents for water disinfection, wound healing, as antibacterial coatings in textiles and food packaging indus-

tries.<sup>5–7</sup> However, the toxicity associated with silver nanoparticles toward the host has raised questions for translating these nanoparticles into antibacterial drugs.<sup>8</sup> Near-infrared (NIR) responsive photothermal property of gold nanoparticles has also been explored for photothermal inactivation of bacteria.<sup>9–11</sup> Apart from metal nanoparticles, the class of two-dimensional (2-D) nanomaterials has attracted a great deal of attention in the past decade as potential antibacterial agents.<sup>12</sup> In this category, graphene-based nanomaterials have been studied extensively, which have laid the foundation for antibacterial applications of 2D-nanosheets.<sup>13–18</sup> Recently,

Received: February 13, 2019

Accepted: May 22, 2019

Published: May 22, 2019

another 2D-material, molybdenum disulfide ( $\text{MoS}_2$ ), has emerged as a potent nanomedicine candidate, which has led to its application in the areas of drug delivery, phototherapy, biosensing, water disinfection, and antibacterial wound healing.<sup>19–24</sup> Studies carried out so far have reported the development of a number of functionalized  $\text{MoS}_2$  based nanocomposites for antibacterial applications. In a majority of these reported works,  $\text{MoS}_2$  nanosheets were functionalized either with hydrophobic ligands<sup>25,26</sup> or antimicrobial peptides,<sup>27</sup> or loaded with antibiotics<sup>28</sup> to develop nanocomposites for potential applications in wound healing and water disinfection. In addition to surface functionalization, the NIR responsiveness and peroxidase-like activity of  $\text{MoS}_2$  nanosheets have also been combined with the above functionalities for developing stimulus-responsive photothermal and photocatalytic disinfection systems.<sup>29–32</sup> Similarly, combination with other antibacterial nanomaterials such as silver, graphene oxide,  $\text{Ti}_3\text{C}_2\text{MXene}$ , etc. have also been explored to develop more potent  $\text{MoS}_2$  based antibacterial nanocomposites.<sup>33–35</sup> However, in almost all of the above-mentioned works, it was observed that the antibacterial efficiency of the  $\text{MoS}_2$  nanosheets themselves without its functionalization/loading with antimicrobial agents or in the absence of external stimulus such as NIR light was either very weak or negligible in comparison to the nanocomposite as a whole. For example, functionalization of  $\text{MoS}_2$  nanosheets with thiolated ligands of varying hydrophobicity and charge was found to be very effective against Gram-negative and positive ESKAPE pathogens in comparison to their nonfunctionalized counterparts.<sup>25,26</sup> Recently, the activity of these  $\text{MoS}_2$  nanosheets functionalized with negatively charged thiolated ligands in inhibiting the action of  $\beta$ -lactamase enzyme and thereby improving the sensitivity of multidrug resistant bacteria to  $\beta$ -lactam antibiotics has been demonstrated, which again highlights the prominent role of these ligands in achieving the desired antibacterial action in comparison to the nanosheets themselves.<sup>36</sup> Chemically exfoliated  $\text{MoS}_2$  nanosheets (ce- $\text{MoS}_2$ ) functionalized with chitosan and loaded with an antibiotic were found to be very effective against Gram-positive bacterium *S. aureus* and its biofilm.<sup>28</sup> However, the authors reported that the chitosan functionalized  $\text{MoS}_2$  nanosheets themselves did not contribute directly toward the antibacterial activity and that the activity was due to the entrapment of the bacteria by the nanosheets followed by subsequent release of the antibiotics into the vicinity of the trapped cells. The intrinsic antibacterial potential of the chitosan functionalized nanosheets was not addressed. Zhang et al. reported a chitosan functionalized magnetic  $\text{MoS}_2$  nanocomposite loaded with iron oxide nanoparticles, which showed high antibacterial effect through a combined action of magnetic field assisted bacterial enrichment and NIR mediated heat generation.<sup>32</sup> However, in the absence of a magnetic field and without NIR irradiation, the functionalized  $\text{MoS}_2$  nanosheets showed negligible antibacterial activity. Similarly, in another work reported by Feng et al., the photothermal and photodynamic effect of chitosan functionalized  $\text{MoS}_2$  nanosheets deposited on a titanium substrate was evaluated against Gram-negative and Gram-positive bacteria under the exposure of visible and NIR light.<sup>30</sup> The functionalized substrate showed excellent antibacterial potential in the presence of dual-light irradiation; however, in the absence of irradiation, the antibacterial activity of the substrate was feeble. Thus, all these results showed that additional functionalization or

external stimulus played a more prominent role in achieving the desired antibacterial action, whereas the actual intrinsic potential of the  $\text{MoS}_2$  nanosheets or chitosan functionalized  $\text{MoS}_2$  nanosheets themselves was not investigated and realized in detail.

Here, in this work we have addressed this specific aspect by evaluating the antibacterial potential of chitosan functionalized  $\text{MoS}_2$  nanosheets exclusively. To date, there has been only a single report on the antibacterial activity of chemically exfoliated  $\text{MoS}_2$  nanosheets (ce- $\text{MoS}_2$ ) without any functionalization.<sup>37</sup> The study showed the growth inhibitory effect of ce- $\text{MoS}_2$  nanosheets on *E. coli* at high concentrations and reported on the ability of ce- $\text{MoS}_2$  nanosheets to produce abiotic oxidative stress. However, a detailed understanding of the mechanism of action of these nanosheets was not addressed. As a result, we have also tried to decipher the exact mechanism of antibacterial action of the chitosan exfoliated  $\text{MoS}_2$  nanosheets in a systematic manner to provide a better understanding of the events occurring both at the membrane surface as well as inside the bacterial cells as a consequence of nanosheet interaction with the bacteria. Molecular simulation studies to understand the interactions of  $\text{MoS}_2$  nanosheets with bacterial membrane have recently reported the role of  $\text{MoS}_2$  nanosheets in causing extensive membrane damage through dent formation and phospholipid extraction.<sup>38</sup> However, none of the reported works so far has investigated the intracellular processes occurring inside bacterial cells as a consequence of  $\text{MoS}_2$  nanosheet interaction, which might contribute together with membrane damage for achieving the bactericidal action. Also, the possibility of involvement of intracellular biotic oxidative stress in addition to abiotic stress toward the overall antibacterial activity of  $\text{MoS}_2$  nanosheets has also not been investigated.

Herein, we report the detailed antibacterial mechanism of chitosan exfoliated  $\text{MoS}_2$  nanosheets (CS- $\text{MoS}_2$ ) synthesized by a one-step, green method of aqueous chitosan solution assisted exfoliation without the use of any chemicals. First, the antibacterial potential of the CS- $\text{MoS}_2$  nanosheets without any additional surface functionalization with complex ligands, biocidal nanoparticles, photosensitizers, or antibiotics, and in the absence of any external stimulus such as NIR light, was evaluated against both Gram-negative and positive bacteria. Next, through a set of carefully designed experiments, we investigated the effect of CS- $\text{MoS}_2$  nanosheets on the membrane structure and integrity of bacterial cells. Through a combination of qualitative and quantitative techniques such as fluorescent dye-based assays, fluorescence microscopy, and scanning electron microscopy, we deciphered the processes of membrane depolarization and physical disruption of lipid bilayer occurring in the bacterial cells as a result of CS- $\text{MoS}_2$  nanosheet interaction with the membranes. We then extended our investigations into understanding the intracellular events happening as a result of membrane damage and studied its effect on bacterial respiration, metabolism, and prooxidant–antioxidant equilibrium. Once the mechanism was successfully deciphered, we then focused on evaluating the therapeutic potential of CS- $\text{MoS}_2$  nanosheets by analyzing its antibiofilm properties and cytotoxicity toward mammalian cells. Our results indicate that CS- $\text{MoS}_2$  nanosheets are highly efficient antibacterial and antibiofilm agents with a high degree of biocompatibility toward mammalian cells, and the observed antibacterial action of these nanosheets is a result of the

combined action of membrane damage, metabolic inactivation, and oxidative stress.

## 2. MATERIALS AND METHODS

**2.1. Materials.** Molybdenum(IV) sulfide, chitosan, acetic acid, propidium iodide, glutaraldehyde, 2,7-dichlorofluorescein diacetate, cell proliferation assay kit II (XTT), and Bradford reagent were purchased from Sigma-Aldrich. 3,3'-Dipropylthiadcarbocyanine iodide, S (and 6)-carboxyfluorescein diacetate succinimidyl ester, S,S-dithio-bis(2-nitrobenzoic acid), and resazurin sodium salt were obtained from TCI Co. Ltd. Luria-Bertani broth and ethanol were purchased from Merck. HEPES buffer was obtained from SRL Pvt. Ltd. Pierce LDH Cytotoxicity Assay Kit, fetal bovine serum (FBS), DMEM culture medium, 0.25% trypsin-ethylenediaminetetraacetic acid (EDTA), and penicillin-streptomycin (Pen Strep) were obtained from Gibco (Thermo Scientific). All reagents were used as received. Milli-Q ultrapure water was used in all experiments.

**2.2. Synthesis of CS-MoS<sub>2</sub> Nanosheets.** The CS-MoS<sub>2</sub> nanosheets were synthesized by exfoliating bulk MoS<sub>2</sub> in an aqueous solution of chitosan using ultrasonication. Briefly, a chitosan stock solution of 5 mg/mL was prepared in 0.2% acetic acid solution. Then 60 mg of bulk MoS<sub>2</sub> powder was added to 12 mL of 5 mg/mL chitosan solution and 18 mL of deionized water to make the final reaction volume to 30 mL. The bulk MoS<sub>2</sub> powder was first dispersed in the aqueous chitosan solution by bath sonication it for 20 min and then exfoliated into nanosheets by probe sonication for 4 h with a 15 min on/off cycle. Following sonication, the solution was centrifuged at 5000 rpm for 45 min, and the supernatant containing the exfoliated nanosheets was collected. The pellet having unexfoliated or bulk MoS<sub>2</sub> was discarded. The obtained supernatant was then subjected to a second round of centrifugation at 10 000 rpm for 30 min to remove the excess or free chitosan. The supernatant was discarded, and the pellet was redispersed in deionized water to obtain a clear homogeneous dark green solution of CS-MoS<sub>2</sub> nanosheets.

**2.3. Characterization.** The UV-vis spectra were recorded with a UV-1800 spectrophotometer (Shimadzu, Japan). Fourier transform infrared (FT-IR) spectra measurements of the bulk MoS<sub>2</sub>, pure chitosan, and CS-MoS<sub>2</sub> nanosheet powder were performed with K8002AA carry 660 FTIR (Agilent Technologies). X-ray diffraction (XRD) of bulk MoS<sub>2</sub>, pure chitosan, and CS-MoS<sub>2</sub> nanosheet powder was measured with a Rigaku SmartLab 9 kW rotating anode X-ray diffractometer. The thermal decomposition profiles of bulk MoS<sub>2</sub>, pure chitosan, and CS-MoS<sub>2</sub> nanosheet powder were obtained using a thermal gravimetric analyzer (Pyris 1 TGA, PerkinElmer) operated in the temperature range of 25–600 °C at a heating rate of 10 °C/min under nitrogen atmosphere. Raman spectra were obtained using LabRAM HR evolution Raman spectrometer equipped with a 785 nm laser (Horiba). X-ray photoelectron spectroscopy (XPS) measurements were recorded using Thermo NEXSA Surface Analysis and the data was analyzed using Thermo Avantage v5.9908. The morphology and size of CS-MoS<sub>2</sub> nanosheets were studied by transmission electron microscopy (TEM, FP 5022/22-Tecnai G2 20 S-TWIN, FEI) and scanning electron microscopy (SEM, Nova Nano SEM-450, FEI). The zeta potential of bulk MoS<sub>2</sub> and CS-MoS<sub>2</sub> nanosheet was measured by Zetasizer Nano ZS (Malvern, UK).

**2.4. Bacterial Strain and Growth Conditions.** The bacterial strains used in this study include ampicillin resistant Gram-negative bacterium *Escherichia coli* (*E. coli*) and Gram-positive bacterium *Staphylococcus aureus* (*S. aureus*) (MTCC 96). Both *E. coli* and *S. aureus* were grown in Luria-Bertani (LB) broth at 37 °C and 180 rpm for 12 h and then subcultured in LB broth and stored at 4 °C for future use.

**2.5. Assay for Antibacterial Activity of CS-MoS<sub>2</sub> Nanosheets.** The antibacterial activity of the synthesized CS-MoS<sub>2</sub> nanosheets against *E. coli* and *S. aureus* was analyzed using bacterial growth kinetics. Bacteria were grown in fresh LB media incorporated with increasing concentrations of CS-MoS<sub>2</sub> nanosheets (10–160 µg/mL) for 12 h. The growth of untreated and treated cells was monitored periodically by measuring absorbance at 600 nm in a

spectrophotometer and was expressed as percentage growth of treated cells as compared to control (untreated cells).

**2.6. Minimum Inhibitory Concentration (MIC) and Minimum Bactericidal Concentration (MBC).** The minimum inhibitory concentration (MIC) and minimum bactericidal concentration (MBC) of CS-MoS<sub>2</sub> nanosheets against *E. coli* and *S. aureus* were evaluated by a standard 96-well microbroth dilution assay. Bacteria were inoculated into 200 µL of LB broth at 1% v/v level in micro titer wells and grown overnight at 37 °C and 180 rpm in the presence of increasing concentrations of the CS-MoS<sub>2</sub> nanosheets. The growth of treated cells was monitored by measuring OD at 600 nm in a microplate reader (Tecan Infinite M200 Pro). The lowest concentration of the CS-MoS<sub>2</sub> nanosheets that resulted in an OD<sub>600</sub> reading of less than 0.1, indicating lack of cell growth, was considered as the MIC value.

For determination of MBC, all culture wells that showed OD<sub>600</sub> ≤ 0.1 were reinoculated into fresh 200 µL of LB broth in absence of CS-MoS<sub>2</sub> nanosheets at 1% v/v level and allowed to grow for a further period 12 h at 37 °C and 180 rpm. Now, the lowest concentration of the CS-MoS<sub>2</sub> nanosheets that resulted in an OD<sub>600</sub> reading of less than 0.1 (complete prevention of growth) following reinoculation was taken as the MBC value. The MIC and MBC values were calculated from three independent experiments.

**2.7. Membrane Depolarization Assay.** *E. coli* and *S. aureus* cells in their mid log phase (OD<sub>600</sub> = 0.4–0.5) were washed with a buffer solution (5 mM HEPES buffer, 5 mM glucose, pH 7.2) and redispersed in the same buffer to an OD<sub>600</sub> of 0.1. The redispersed cells were then incubated with 0.4 µM of 3,3'-dipropylthiadcarbocyanine iodide (diSC35) dye for 1 h at 37 °C in a 96-well plate, following which 100 mM KCl was added to the suspensions.<sup>39</sup> After incubation with dye, the *E. coli* and *S. aureus* cells were treated with CS-MoS<sub>2</sub> nanosheets at their respective MIC concentrations, and the fluorescence of the treated cells was monitored periodically over a period of 1 h in a microplate reader (Tecan Infinite M200 Pro) set to an excitation wavelength of 622 nm and emission wavelength of 670 nm. Increase in fluorescence with time indicates membrane depolarization.

**2.8. Assays for Studying Membrane Damage.** The effect of CS-MoS<sub>2</sub> nanosheets on the integrity of bacterial membranes was evaluated by (1) cFDA/SE leakage assay, (2) PI uptake assay, (3) cFDA/SE-PI dual stain fluorescence microscopy assay, and (4) protein leakage assay.

**2.8.1. cFDA/SE Leakage Assay.** *E. coli* and *S. aureus* cells (10<sup>6</sup> CFU/mL) suspended in sterile PBS were stained with 50 µM of 5 (and 6)-carboxyfluorescein diacetate succinimidyl ester (cFDA-SE) dye for 20 min at 37 °C.<sup>39</sup> The stained cells were then washed twice with sterile PBS to remove excess dye and resuspended in PBS containing increasing concentrations of CS-MoS<sub>2</sub> nanosheets. The cFDA-SE dye stained cells were treated with CS-MoS<sub>2</sub> nanosheets for 6 h at 37 °C and 200 rpm, following which the suspensions were centrifuged at 6000 rpm for 5 min, and the fluorescence of the collected supernatants containing the leaked dye molecules was measured at an excitation wavelength of 488 nm and emission wavelength of 518 nm in a spectrofluorimeter. *E. coli* were treated with CS-MoS<sub>2</sub> nanosheets at MIC, 2 × MIC, 4 × MIC, and 6 × MIC values, whereas *S. aureus* were treated at their MIC, 1.5 × MIC, 2 × MIC, and 2.5 × MIC values. Control cells were stained with the dye and incubated under similar conditions in the absence of CS-MoS<sub>2</sub> nanosheets. The fluorescence measurements were recorded after the fluorescence of effluxed dye from control samples was subtracted. Fluorescence measurements were taken for three independent samples.

**2.8.2. PI Uptake Assay.** *E. coli* and *S. aureus* cells (10<sup>6</sup> CFU/mL) were treated with increasing concentrations of CS-MoS<sub>2</sub> nanosheets for 6 h at 37 °C and 200 rpm, following which the suspensions were centrifuged at 6000 rpm for 5 min. The obtained cell pellets were then stained with 30 µM propidium iodide (PI) dye for 30 min at 37 °C.<sup>39</sup> The stained cells were then washed in PBS to remove excess PI molecules and redispersed in same buffer. *E. coli* were treated with CS-MoS<sub>2</sub> nanosheets at MIC, 2 × MIC, 4 × MIC, and 6 × MIC

values, whereas *S. aureus* were treated at their MIC,  $1.5 \times$  MIC,  $2 \times$  MIC, and  $2.5 \times$  MIC values. Control cells were stained with the dye and incubated under similar conditions without any treatment with CS-MoS<sub>2</sub> nanosheets. The fluorescence was measured in a spectrofluorimeter at an excitation wavelength of 535 nm and emission wavelength of 617 nm. The fluorescence measurements were recorded after the fluorescence obtained from control samples was subtracted. Fluorescence measurements were taken for three independent samples.

**2.8.3. cFDA/SE-PI Dual Stain Fluorescence Microscopy.** *E. coli* and *S. aureus* cells ( $10^6$  CFU/mL) were treated with increasing concentrations of CS-MoS<sub>2</sub> nanosheets for 6 h at 37 °C and 200 rpm. Following treatment, the cells were washed twice with PBS and both control and treated cells were stained with cFDA/SE and PI as mentioned earlier. After being washed to remove excess stains, stained cells were fixed in 2.5% glutaraldehyde, and then 10 μL of the fixed cells suspended in PBS was drop-casted on a clean glass slide, air-dried, and observed under a fluorescence microscope equipped with a blue and green laser. Fluorescence images of the cells were recorded.

**2.8.4. Protein Leakage Assay.** *E. coli* and *S. aureus* cells ( $10^6$  CFU/mL) were treated with increasing concentrations of CS-MoS<sub>2</sub> nanosheets for 6 h at 37 °C and 200 rpm. Following treatment, the cells were pelleted down at 5000 rpm for 5 min, and the cell-free supernatant was collected. The concentration of leaked proteins in the supernatant was measured using standard Bradford assay.

**2.9. Scanning Electron Microscopy (SEM) Analysis.** The effect of CS-MoS<sub>2</sub> nanosheets on the cellular morphology of *E. coli* and *S. aureus* cells and the extent of membrane damage were studied by SEM. Then  $10^6$  CFU/mL of *E. coli* and *S. aureus* cells suspended in PBS were treated with CS-MoS<sub>2</sub> nanosheets at their respective MIC values for 6 h at 37 °C and 200 rpm. Following treatment, the cells were pelleted down at 5000 rpm for 5 min and fixed with 3% glutaraldehyde for 1 h at 4 °C. The fixed cells were centrifuged and dehydrated using ethanol gradient (20%, 50%, 70%, 90%, 100%). The dehydrated cells were then drop casted on a cleaned silicon wafer, air-dried, sputter-coated with gold, and observed under SEM. Control cells were also processed in the same manner without being treated with CS-MoS<sub>2</sub> nanosheets.

**2.10. Measurement of Respiratory Dehydrogenase Enzyme (LDH) Activity.** The activity of LDH enzyme in control and treated cells was measured using Pierce LDH Cytotoxicity Assay Kit. Then  $10^6$  CFU/mL of *E. coli* and *S. aureus* cells were treated with increasing concentrations of CS-MoS<sub>2</sub> nanosheets for 6 h at 37 °C and 200 rpm. Following treatment, the cells were pelleted down at 5000 rpm for 5 min and supernatant was discarded. The pellet was washed with PBS and incubated with LDH reaction solution for 30 min in dark for the formation of red formazan. The reaction was stopped by adding stop solution, and then the absorbance of the solutions was measured at 490 nm using a microplate reader (Tecan Infinite M200 Pro). The results were plotted as % LDH activity of treated cells with respect to control.

**2.11. Measurement of Metabolic Activity.** The metabolic activity of cells was measured using Alamar blue assay which is based on the ability of cells to convert a purple nonfluorescent dye resazurin to its pink fluorescent reduced form resofurin.<sup>40,41</sup> Then  $10^6$  CFU/mL of *E. coli* and *S. aureus* cells were treated with increasing concentrations of CS-MoS<sub>2</sub> nanosheets for 6 h at 37 °C and 200 rpm. Both control and treated cells were incubated with 25 μL of 50 μg/mL resazurin solution for 1 h at 37 °C. The metabolic conversion of resazurin to pink colored resofurin was quantified spectrophotometrically by measuring absorbance at 571 nm.

**2.12. Measurement of Intracellular ROS Production.** Intracellular ROS was measured using standard 2,7-dichlorofluorescein diacetate (DCFH-DA) assay.<sup>40</sup> Then  $10^6$  CFU/mL of *E. coli* and *S. aureus* cells were treated with increasing concentrations of CS-MoS<sub>2</sub> nanosheets for 6 h at 37 °C and 200 rpm. Following treatment, both control and treated cells were washed with PBS and incubated with 100 μM DCFH-DA probe for 30 min in dark at 37 °C. The green fluorescence originating from the oxidative cleavage of DCFH-DA to DCF was measured in a microplate reader (Tecan Infinite M200 Pro)

with an excitation wavelength of 485 nm and emission wavelength of 528 nm. The fold increase in intracellular ROS production in cells treated with CS-MoS<sub>2</sub> nanosheets in comparison to control cells was plotted.

**2.13. Measurement of Intracellular Glutathione (GSH) Activity.** The activity of intracellular GSH was determined using standard Ellman's assay as widely reported in literature.<sup>26,40</sup> Then  $10^6$  CFU/mL of *E. coli* and *S. aureus* cells were treated with increasing concentrations of CS-MoS<sub>2</sub> nanosheets for 6 h at 37 °C and 200 rpm. Following treatment, both control and treated cells were centrifuged at 5000 rpm for 5 min, washed with PBS, and lysed. The lysed cells were further centrifuged, and the clear supernatant was collected. The supernatant was mixed with 50 mM Tris-HCl and 100 mM 5,5-dithio-bis(2-nitrobenzoic acid) (DTNB) and incubated for 30 min in dark at 37 °C. The absorbance of the resulting solution was measured at 412 nm using a UV-visible spectrometer. The percentage loss of glutathione was calculated as

$$\left( 1 - \frac{OD@412\text{ nm of treated}}{OD@412\text{ nm of control}} \right) \times 100$$

**2.14. Biofilm Viability Assay.** *S. aureus* biofilms were grown in 96-well microtiter plates according to a reported method.<sup>42</sup> Following 48 h of biofilm growth, the media were replaced with fresh media containing increasing concentrations of CS-MoS<sub>2</sub> nanosheets (MIC,  $1.5 \times$  MIC,  $2 \times$  MIC,  $2.5 \times$  MIC). The biofilms were treated with the nanosheets for 24 h at 37 °C in a moist environment under static conditions. Following 24 h of treatment, the media were removed from the wells, and the biofilms were washed twice with PBS carefully to remove planktonic cells. The viability of the biofilms was measured using Resazurin reduction test. Then 100 μL of LB broth containing 10 μL of 5 μg/mL resazurin was added to the wells, and the plate was incubated for 45 min at 37 °C. Fluorescence was measured in microplate reader (Tecan Infinite M200 Pro) at 571 nm excitation and 590 nm emission. The % viability of the treated biofilms with respect to control was calculated and plotted.

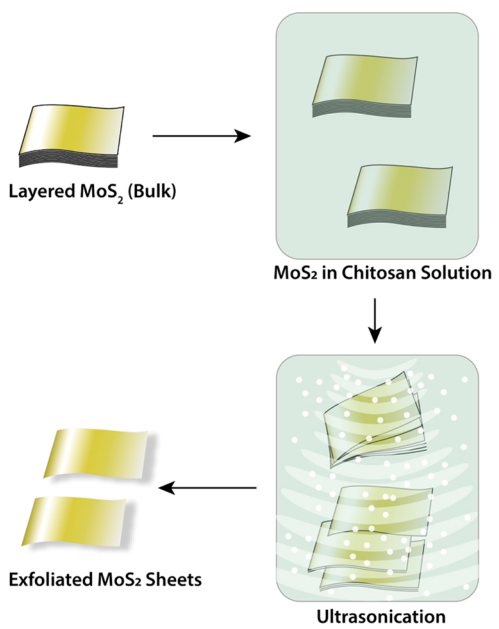
**2.15. In Vitro Cytotoxicity of CS-MoS<sub>2</sub> Nanosheets.** The *in vitro* cytotoxicity or biocompatibility of CS-MoS<sub>2</sub> nanosheets was evaluated against the mammalian kidney cell line HEK-293A and breast cancer cell line MCF-7 by XTT assay according to manufacturer's protocol. HEK-293A and MCF-7 cells were allowed to grow overnight in 96-well plates at a density of 10 000 cells/well. The adhered cells were treated with increasing concentrations of CS-MoS<sub>2</sub> nanosheets (10–200 μg/mL) and incubated for 24 h at 37 °C and under 5% CO<sub>2</sub> in an incubator. Cells without any treatment were used as controls. Following treatment, 80 μL of XTT reagent was added to each well and incubated for 2 h at 37 °C. Absorbance of the plate was measured at 490 and 690 nm using a plate reader (Tecan Infinite M200 Pro). Absorbance values of each well at 690 nm was subtracted from that of 490 nm to minimize the background absorbance of media. Each experiment was performed in triplicate and values were reported as mean ± SD. The % cell viability was calculated using the following equation:

$$\frac{\text{Absorbance of treated cells}}{\text{Absorbance of control cells}} \times 100$$

### 3. RESULTS AND DISCUSSION

**3.1. Synthesis and Characterization of CS-MoS<sub>2</sub> Nanosheets.** A simple, one-step, green process of chitosan assisted exfoliation and stabilization was adopted for the synthesis of CS-MoS<sub>2</sub> nanosheets. The synthesis process did not involve the use of any harsh chemicals like lithium, oleum, or other organic solvents that are commonly used for the synthesis of MoS<sub>2</sub> nanosheets. The present synthesis process involved ultrasonication mediated exfoliation of bulk MoS<sub>2</sub> powder in an aqueous solution of chitosan and simultaneous stabilization (Scheme 1). The process of stripping off the

**Scheme 1.** Schematic Showing Synthesis of CS-MoS<sub>2</sub> Nanosheets



multiple layers of bulk MoS<sub>2</sub> into single or few-layered 2D nanosheets was carried out by the combined effects of chitosan and ultrasonication. Chitosan participated in weakening the

van der Waals interactions between the layers in the bulk material by intercalating between them, thus enabling the exfoliation of the bulk MoS<sub>2</sub> into individual sheets during ultrasonication.<sup>43</sup> The use of high frequency ultrasound waves helped in achieving a highly efficient exfoliation of bulk MoS<sub>2</sub> by the action of acoustic cavitation. The propagation of high frequency sonic waves through the aqueous solvent resulted in the creation of cavities or bubbles in close vicinity of the bulk material. These bubbles grew in size over time and ultimately collapsed violently creating high-speed jets and intense shock-waves, either at the vicinity or on the surface of the layered material.<sup>43</sup> As a result, these intense energy pockets finally caused the separation of the already loosened layers of the bulk material into individual sheets. In addition to exfoliation, the process of ultrasonication also helped in reducing the size of the exfoliated MoS<sub>2</sub> sheets to the nanoscale range by breaking the sheets along the defects generated by acoustic cavitation. Incorporation of chitosan directly during the process of exfoliation helped in achieving a highly stable aqueous dispersion of MoS<sub>2</sub> nanosheets. Owing to their hydrophobic nature, MoS<sub>2</sub> nanosheets are known to form aggregates in solution through hydrophobic interactions among themselves. This problem was overcome by the use of the cationic polymer chitosan, which interacted with the negatively charged exfoliated MoS<sub>2</sub> nanosheets in solution and stabilized them by adsorbing on the surface of the sheets. This decreased the hydrophobic interaction among the sheets, thereby preventing the restacking of the sheets and also improved the

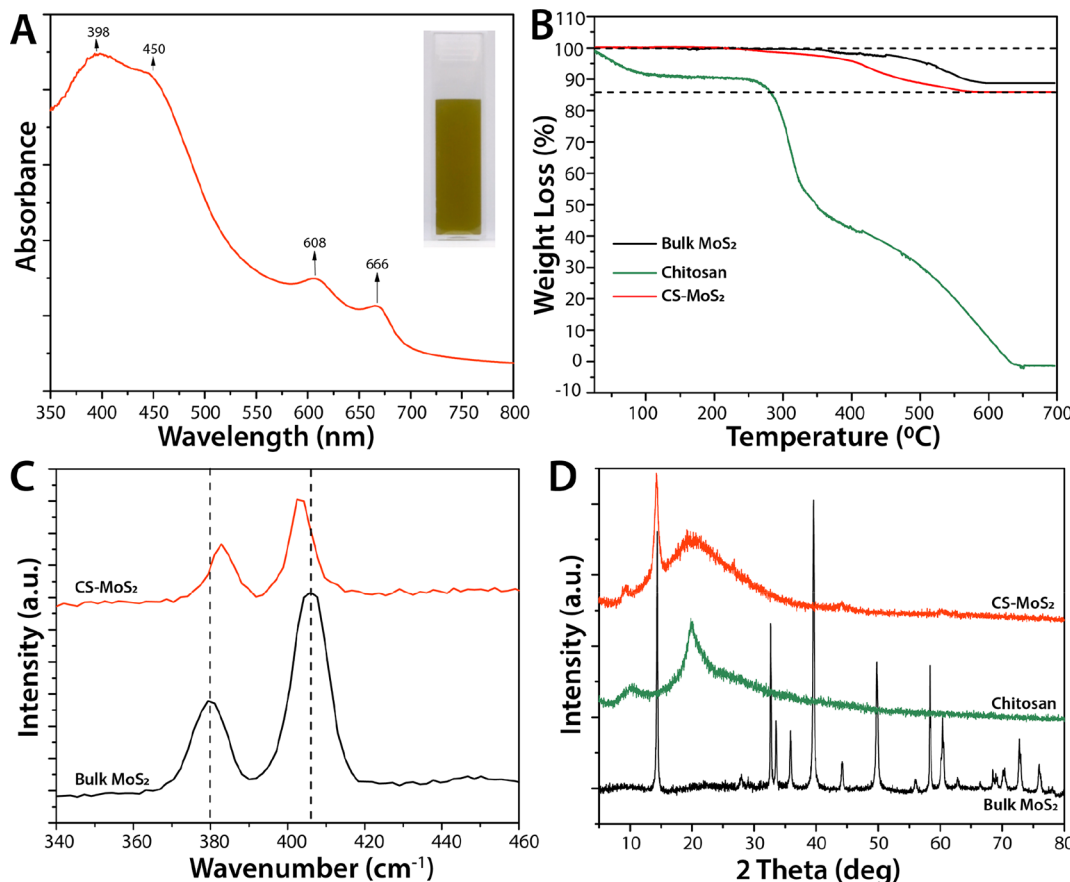


**Figure 1.** Spectroscopic characterization of CS-MoS<sub>2</sub> nanosheets. (A) UV-vis absorbance spectra of CS-MoS<sub>2</sub> nanosheets; (B) TGA curves of bulk MoS<sub>2</sub>, pure chitosan, and CS-MoS<sub>2</sub> nanosheets; (C) Raman spectra of bulk MoS<sub>2</sub> and CS-MoS<sub>2</sub> nanosheets; and (D) XRD pattern of bulk MoS<sub>2</sub>, pure chitosan, and CS-MoS<sub>2</sub> nanosheets.

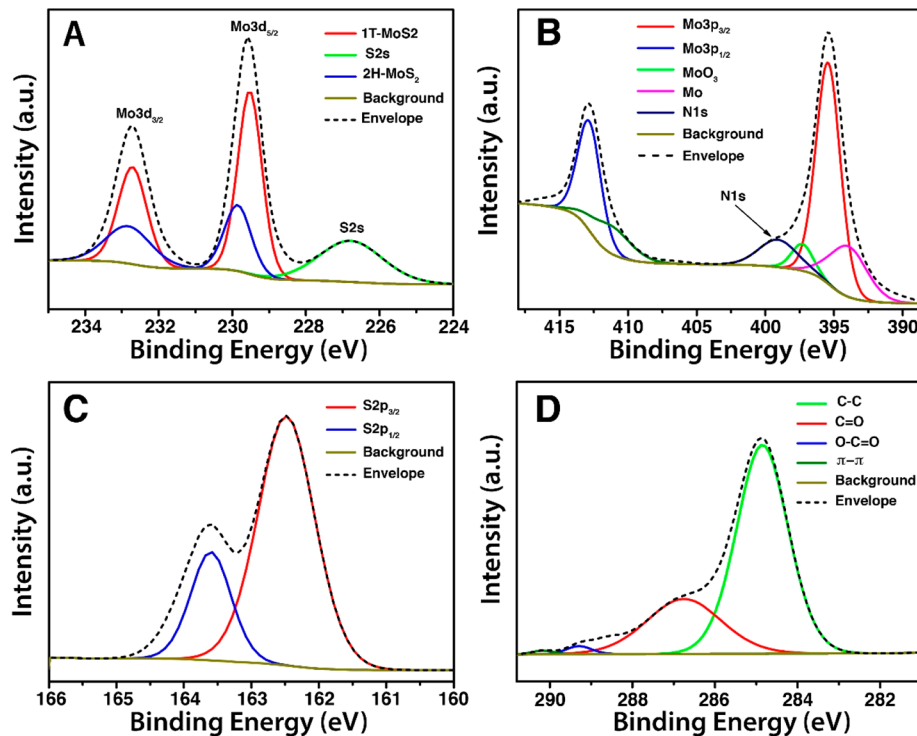


**Figure 2.** XPS analysis of CS-MoS<sub>2</sub> nanosheets. (A) Mo 3d, (B) Mo 3p, (C) S 2p, and (D) C 1s high-resolution spectra of CS-MoS<sub>2</sub> nanosheets.

physiological stability of the nanosheets in aqueous solution. After removing the unexfoliated bulk material and excess chitosan molecules through centrifugation steps, a homogeneous and dark green suspension was obtained, which contained the CS-MoS<sub>2</sub> nanosheets. The as-obtained CS-MoS<sub>2</sub> suspension was further used for detailed characterization and evaluation of its antibacterial potential.

Figure 1A shows the UV-vis absorption spectra of the CS-MoS<sub>2</sub> nanosheet suspension. The spectra clearly depict the characteristic absorption bands at 666, 608, 450, and 398 nm corresponding to single or few-layered 2H-MoS<sub>2</sub>, which proved the successful exfoliation of the bulk material into sheets.<sup>44,45</sup> The bands at 666 and 608 nm arise from direct excitonic transitions at the K point of Brillouin zone, whereas the bands at 450 and 398 nm can be attributed to the direct excitonic transitions at the M point of Brillouin zone.<sup>44</sup> The absorbance spectrum of chitosan solution is provided in Figure S1A. The stabilization of the exfoliated nanosheets with chitosan was investigated using Fourier transform-infrared spectroscopy (FT-IR) and thermal gravimetric analysis (TGA). Figure S1B shows the FT-IR spectrum of bulk MoS<sub>2</sub>, pure chitosan, and CS-MoS<sub>2</sub> nanosheets. From the figure, it is clearly evident that CS-MoS<sub>2</sub> nanosheets showed an absorption spectrum similar to that of pure chitosan molecules. Peaks centered around 1320–1650 cm<sup>-1</sup> and 2840–2960 cm<sup>-1</sup> could be observed in the spectra of both CS-MoS<sub>2</sub> and pure chitosan, which originated from the internal stretching vibrations of amide bonds and –CH<sub>2</sub>– stretching vibrations of chitosan molecules, respectively.<sup>46</sup> In addition, sharp peaks around 1000–1070 cm<sup>-1</sup> corresponding to stretching vibrations of C–O bond were also observed in the spectra of both CS-MoS<sub>2</sub> and pure chitosan.<sup>47</sup> Pure chitosan showed two characteristic peaks at 1646 and 1557 cm<sup>-1</sup>, which are assigned to –C=O stretching of amide groups and –NH bending of secondary amide, respectively.<sup>47,48</sup> Along with these two peaks, the FT-IR

spectrum of CS-MoS<sub>2</sub> nanosheets also showed the emergence of a new peak at 1722 cm<sup>-1</sup> that corresponded to the C=O stretching band of carboxyl groups.<sup>48</sup> Furthermore, a hump around 3000–3600 cm<sup>-1</sup> originating from the stretching vibrations of N–H and O–H bonds was present in case of CS-MoS<sub>2</sub> and pure chitosan but completely absent in the spectrum of bulk MoS<sub>2</sub>.<sup>46,48</sup> Thermogravimetric analysis (TGA) of the CS-MoS<sub>2</sub> nanosheets further supported the FT-IR results. As shown in Figure 1B, the TGA curve of bulk MoS<sub>2</sub> showed weight loss between 450 and 550 °C due to the oxidation of MoS<sub>2</sub> to MoO<sub>3</sub>.<sup>48</sup> Chitosan showed a typical thermal decomposition profile with a gradual loss of weight from 250 to 600 °C.<sup>48</sup> The weight loss below 150 °C can be attributed to moisture vaporization. The thermal degradation profile of CS-MoS<sub>2</sub> nanosheets was found to be similar to that of chitosan molecules, showing a gradual decrease in weight over the temperature range of 250–600 °C, thus validating the presence of chitosan on the surface of the nanosheets. On the basis of the TGA data, it was estimated that ~14% of chitosan by weight was present in the CS-MoS<sub>2</sub> nanosheets. Surface charge measurements of CS-MoS<sub>2</sub> nanosheets showed a net positive charge (+16.6 mV) as compared to bulk MoS<sub>2</sub>, which had a net negative charge (-42.8 mV). The presence of the positive charge again confirmed the presence of chitosan on the surface of exfoliated nanosheets.

Further validation of the successful exfoliation of MoS<sub>2</sub> was carried out through Raman spectroscopy and XRD, both of which are very sensitive tools for specifically characterizing layered materials. Figure 1C shows the Raman spectra of bulk MoS<sub>2</sub> and CS-MoS<sub>2</sub>. The characteristic E<sup>1</sup><sub>2g</sub> and A<sub>1g</sub> peaks of MoS<sub>2</sub> were observed in both spectra. It has been reported in literature that successful exfoliation of bulk MoS<sub>2</sub> into thin layers is often associated with a shift of E<sup>1</sup><sub>2g</sub> peak to a higher wavenumber and a shift of A<sub>1g</sub> peak to a lower wavenumber accompanied with a decrease in their intensities, as compared

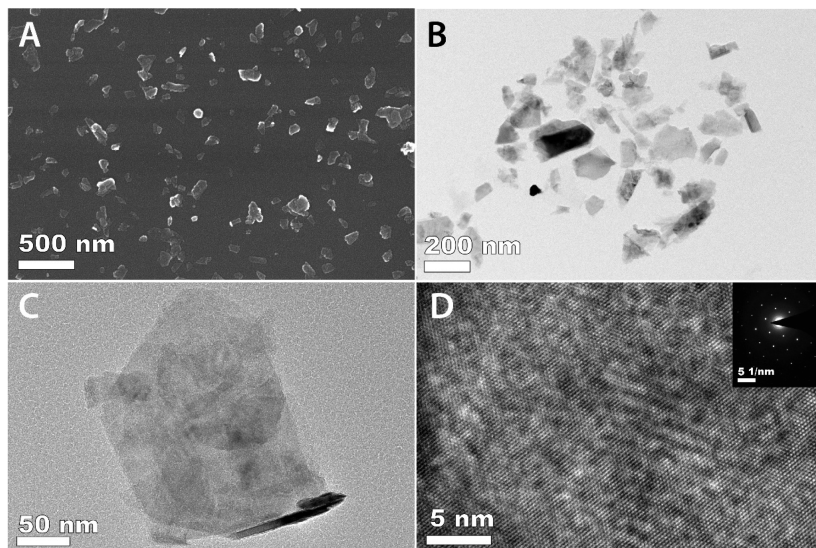


**Figure 3.** Microscopic characterization of CS-MoS<sub>2</sub> nanosheets. (A) SEM of CS-MoS<sub>2</sub> nanosheets, (B, C) TEM of CS-MoS<sub>2</sub> nanosheets, (D) HR-TEM showing high crystallinity of CS-MoS<sub>2</sub> nanosheets. Inset shows the SAED pattern.

to bulk.<sup>44</sup> A careful examination of the Raman spectra obtained with our sample showed a similar pattern. The Raman spectrum of bulk MoS<sub>2</sub> showed the E<sub>2g</sub> and A<sub>1g</sub> peaks at 380 and 406 cm<sup>-1</sup>, respectively. However, the E<sub>2g</sub> peak shifted to 383 cm<sup>-1</sup> and the A<sub>1g</sub> peak shifted to 403 cm<sup>-1</sup> in case of CS-MoS<sub>2</sub>, which clearly confirmed the exfoliation of bulk MoS<sub>2</sub> into thin layers or sheets. XRD analysis of bulk MoS<sub>2</sub>, pure chitosan, and CS-MoS<sub>2</sub> nanosheets as shown in Figure 1D further validated the exfoliation of bulk MoS<sub>2</sub> into single sheets. As can be seen from the figure, the XRD pattern of bulk MoS<sub>2</sub> showed multiple sharp diffraction peaks corresponding to the lattice planes. Chitosan showed one intense XRD peak at ~19.8°. For CS-MoS<sub>2</sub>, the signature XRD peak of MoS<sub>2</sub> at ~14.2° corresponding to the 002 plane of 2H-MoS<sub>2</sub> was clearly observed, however with reduced intensity. This decrease in peak intensity along with broadening confirmed the exfoliated nature of CS-MoS<sub>2</sub>.<sup>47</sup> In addition to this, the characteristic diffraction peak of chitosan at ~19.8° was also observed in the diffraction pattern of CS-MoS<sub>2</sub>, which indicated the presence of the polymer on the sheets. A slight shift in the position of the (002) peak to lower angle was also noticed in case of CS-MoS<sub>2</sub>, which further indicated the interaction of the chitosan molecules with the exfoliated sheets.<sup>47</sup>

Surface composition of the CS-MoS<sub>2</sub> nanosheets was also investigated using XPS analysis and compared with that of chemically exfoliated MoS<sub>2</sub> nanosheets (ce-MoS<sub>2</sub>). The survey spectra of both CS-MoS<sub>2</sub> and ce-MoS<sub>2</sub> confirmed the presence of Mo, S, C, and O elements (Figure S2A). Figures 2A and S2B show the high-resolution Mo 3d spectra of CS-MoS<sub>2</sub> and ce-MoS<sub>2</sub>, respectively. The spectra consist of peaks at 232.73 eV, 229.63 eV, and 226.8 eV corresponding to Mo 3d<sub>3/2</sub>, Mo 3d<sub>5/2</sub>, and S 2s, respectively.<sup>49,50</sup> Deconvolution of the Mo 3d peaks gave rise to additional peaks arising from 1T and 2H phase of MoS<sub>2</sub>. The high-resolution spectra of Mo 3p show two strong peaks at 412.98 and 395.45 eV corresponding to Mo 3p<sub>1/2</sub> and Mo 3p<sub>3/2</sub>, respectively (Figures 2B and S2C).<sup>49,50</sup> As the binding energies of N 1s and Mo 3p overlap with each other, so further deconvolution of the Mo 3p<sub>3/2</sub> peak was carried out, which revealed the presence of three more

peaks in CS-MoS<sub>2</sub> at 399.3 eV, 397.27 eV, and 394.11 eV arising from N 1s, MoO<sub>3</sub>, and Mo (Figure 2B).<sup>51,52</sup> The appearance of a prominent peak corresponding to N 1s further confirmed the presence of chitosan on the surface of the nanosheets, which was found to be completely absent in the high-resolution deconvoluted Mo 3p spectra of ce-MoS<sub>2</sub> nanosheets (Figure S2C).<sup>51</sup> A comparison spectrum of the Mo 3p peak between CS-MoS<sub>2</sub> nanosheets and ce-MoS<sub>2</sub> nanosheets has also been provided in Figure S2D, which clearly shows a prominent hump around 399–400 eV in case of CS-MoS<sub>2</sub> nanosheets, thereby further confirming the presence of nitrogen. The inset provides the difference spectra of this comparison, which again validates the presence of nitrogen in CS-MoS<sub>2</sub> due to the residual chitosan on the nanosheet surface. S 2p spectra were deconvoluted into two prominent peaks at 162.47 and 163.30 eV corresponding to S 2p<sub>3/2</sub> and S 2p<sub>1/2</sub>, respectively (Figures 2C and S2E).<sup>50</sup> In addition, analysis of high-resolution C 1s and O 1s spectra revealed peaks at characteristic binding energies as depicted in Figures 2D and S2F–H.

The morphology and structure of the synthesized CS-MoS<sub>2</sub> nanosheets were next analyzed by scanning electron microscopy (SEM) and transmission electron microscopy (TEM). SEM demonstrated typical sheet-like morphology and high uniformity of the CS-MoS<sub>2</sub> nanosheets (Figure 3A) with an average size of around 126 nm as obtained from the size distribution of the nanosheets (Figure S3). SEM analysis of only chitosan solution showed a typical morphology of polymer distributed on the surface of the substrate forming a layer (Figure S4). Figure 3B and C show TEM images of exfoliated CS-MoS<sub>2</sub> nanosheets. The nanosheets appear uniformly distributed and well dispersed without any signs of aggregation. The presence of single or few layered nanosheets is clearly visible in the images, which again demonstrates the effectiveness of the adopted process in achieving high degree of exfoliation. The nanosheets also exhibited well-defined laminar morphology (Figure 3B,C) and high crystalline nature as evident from the high resolution-TEM (HR-TEM; Figure 3D) and selected area electron diffraction (SAED; Figure 3D inset)

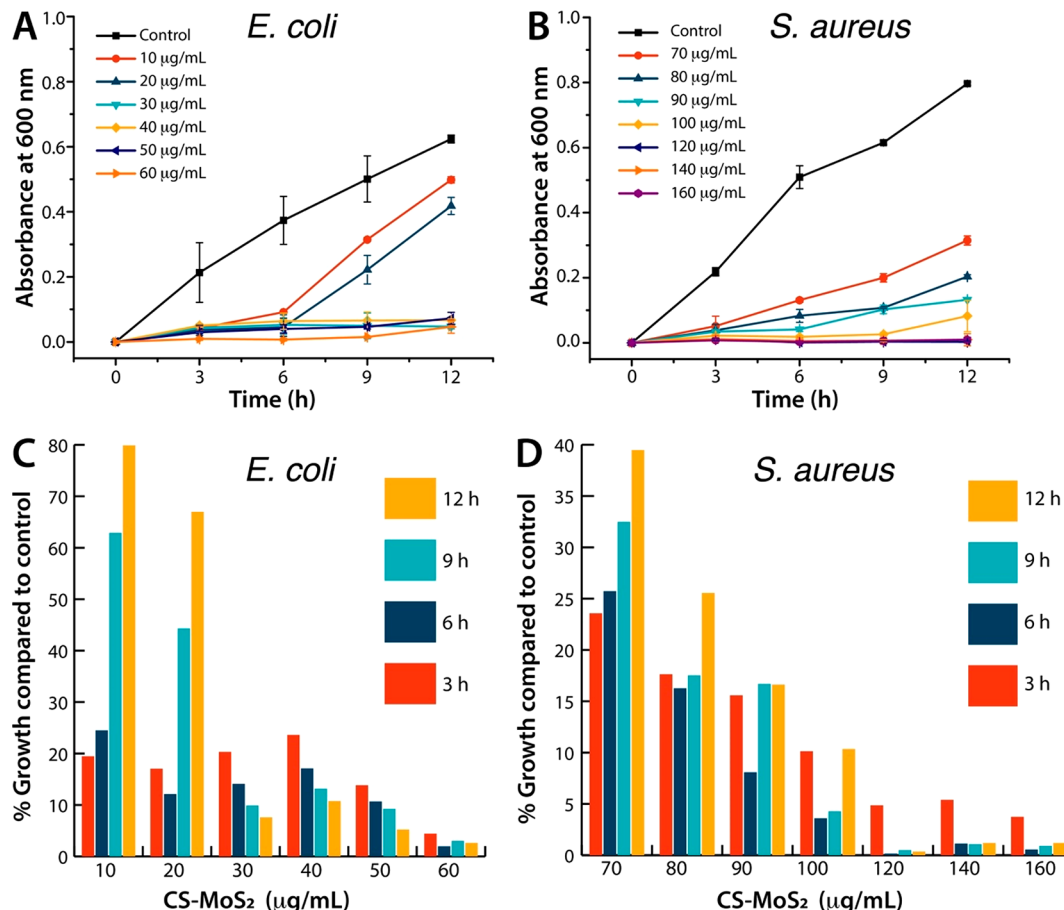


**Figure 4.** Antibacterial activity of CS-MoS<sub>2</sub> nanosheets. Growth kinetics of (A) *E. coli* and (B) *S. aureus* treated with different concentrations of CS-MoS<sub>2</sub> nanosheets. % growth of (C) *E. coli* and (D) *S. aureus* treated with different concentrations of CS-MoS<sub>2</sub> nanosheets.

images.<sup>44</sup> The SAED pattern clearly revealed the hexagonal lattice of the MoS<sub>2</sub> nanosheets.

### 3.2. Antibacterial Activity of CS-MoS<sub>2</sub> Nanosheets.

The antibacterial activity of CS-MoS<sub>2</sub> nanosheets was investigated against Gram-negative ampicillin resistant *E. coli* and Gram-positive *S. aureus* using bacterial growth kinetics. The absorbance of untreated and treated bacterial suspensions was periodically measured at 600 nm and monitored over a period of 12 h. Figure 4A and B show the growth curve of *E. coli* and *S. aureus*, respectively, treated with increasing concentrations of CS-MoS<sub>2</sub> nanosheets. The growth curves clearly show a concentration-dependent antibacterial activity of the synthesized nanosheets against both drug resistant Gram-negative and Gram-positive bacteria. A quantitative evaluation of the antibacterial activity of CS-MoS<sub>2</sub> nanosheets has been represented in Figure 4C and D in the form of percentage growth of treated cells as compared to control. It is evident from the results that CS-MoS<sub>2</sub> nanosheets were highly effective in inhibiting the growth of bacterial cells in a concentration as well as time-dependent manner. It was observed that at a concentration of 30 µg/mL, the CS-MoS<sub>2</sub> nanosheets were able to cause around 80% inhibition in the growth of *E. coli* within 3 h of treatment, which was increased to 96% when the *E. coli* were treated with 60 µg/mL of the nanosheets for the same duration (Figure 4C). It was also found that the antibacterial efficiency of the CS-MoS<sub>2</sub> nanosheets toward *E. coli* improved over time and increased from 80% to 93% after 12 h at the concentration of 30 µg/mL. Furthermore, it is to be

noted that the growth inhibition of *E. coli* was always maintained over 98% throughout the period of 12 h at the concentration of 60 µg/mL, which clearly showed that this concentration of CS-MoS<sub>2</sub> nanosheets was the most efficient in completely retarding the growth of the Gram-negative bacterial cells. Similar concentration- and time-dependent antibacterial activities were also observed against the Gram-positive bacterium *S. aureus*; however, a higher concentration of CS-MoS<sub>2</sub> nanosheets as compared to *E. coli* was found to be effective in inhibiting the growth of *S. aureus* (Figure 4D). It was noticed that around 99% growth inhibition of *S. aureus* by CS-MoS<sub>2</sub> nanosheets was achieved at a concentration of 120 µg/mL. To probe into the role of chitosan present on the surface of nanosheets toward the observed antibacterial action, we carried out similar growth kinetics experiment with chitosan treated *E. coli* and *S. aureus* cells. The TGA results showed that the CS-MoS<sub>2</sub> nanosheets contained around 14% (w/w) chitosan. Therefore, on the basis of these data, the *E. coli* and *S. aureus* cells were treated with increasing concentrations of chitosan corresponding to the CS-MoS<sub>2</sub> nanosheet concentration range used in the antibacterial study. As shown in Figure S5, the results clearly revealed that the amount of chitosan present in the synthesized nanosheets did not contribute toward the observed antibacterial activity with the CS-MoS<sub>2</sub> nanosheets. Hence, it is reasonable to conclude that the antibacterial activity of the synthesized CS-MoS<sub>2</sub> nanosheets against *E. coli* and *S. aureus* is solely due to the direct action of MoS<sub>2</sub> nanosheet, where the

presence of chitosan on the surface of the nanosheets only contributed toward giving stability to the nanosheets in solution and helped in improving the interaction of the MoS<sub>2</sub> nanosheets with bacterial surface through electrostatic interactions.

The minimum inhibitory concentration (MIC) and minimum bactericidal concentration (MBC) of the CS-MoS<sub>2</sub> nanosheets against both *E. coli* and *S. aureus* were calculated using the standard microbroth dilution assay as mentioned in **Materials and Methods** section. The MIC and MBC values of CS-MoS<sub>2</sub> nanosheets against *E. coli* were found to be 30 and 60 µg/mL, respectively. Similarly, for *S. aureus*, the values were reported to be 90 and 120 µg/mL, respectively. The presence of a thick peptidoglycan layer surrounding the Gram-positive bacterial cells may contribute toward the requirement of a higher concentration of CS-MoS<sub>2</sub> for achieving antibacterial activity against *S. aureus*. In addition to this, the bactericidal potential of CS-MoS<sub>2</sub> nanosheets was also evaluated based on the MBC/MIC ratio. The results of MIC, MBC, and bactericidal potential of CS-MoS<sub>2</sub> nanosheets are summarized in **Table 1**. The MBC/MIC ratio is widely considered as a

**Table 1.** MIC, MBC, and MBC/MIC Ratio of CS-MoS<sub>2</sub> Nanosheets

organism	MIC value (µg/mL)	MBC value (µg/mL)	MBC/MIC ratio
<i>E. coli</i>	30	60	2
<i>S. aureus</i>	90	120	1.33

useful parameter to evaluate the bactericidal potential of any antibacterial agent. An agent is considered to be bactericidal if its MBC/MIC ratio is less than or equal to 4.<sup>53</sup> We observed that for both *E. coli* and *S. aureus*, the MBC/MIC ratio of CS-MoS<sub>2</sub> nanosheets was calculated to be much less than 4 (**Table 1**), thereby clearly establishing the bactericidal potential of CS-MoS<sub>2</sub> nanosheets.

**3.3. Mechanism of Antibacterial Action.** **3.3.1. Membrane Depolarization and Loss of Membrane Integrity.** **3.3.1.1. Membrane Depolarization.** Many antibacterial agents have been found to exert their bactericidal effects through destabilization of the transmembrane potential of bacterial cells subsequently leading to the physical disruption of the lipid

bilayer or membrane damage.<sup>39,54</sup> The ability of the synthesized CS-MoS<sub>2</sub> nanosheets to cause membrane depolarization was investigated using a cationic fluorescent dye diSC<sub>3</sub>S, which upon entering cells compartmentalizes itself between the inner and outer layers of the bacterial membrane. In doing so, fluorescence of the dye gets quenched. If the membrane gets depolarized due to the action of any depolarizing agent, the dye comes out of the cells, and as a result, an increase in fluorescence is observed.<sup>54</sup> This increase in fluorescence is measured as an indicator of membrane depolarization. *E. coli* and *S. aureus* cells preincubated with diSC<sub>3</sub>S dye and treated with CS-MoS<sub>2</sub> nanosheets at their respective MIC concentrations displayed a time-dependent increase in the fluorescence intensity of the dye in comparison to dye labeled untreated cells, which clearly indicated that the nanosheets interacted with the bacterial membranes and caused membrane depolarization (**Figure 5**). Recent studies into understanding the nature of interaction of MoS<sub>2</sub> nanosheets with bacterial membrane through computer simulations have revealed that MoS<sub>2</sub> nanosheets attach to the surface of the membrane and embed themselves into the membrane through the formation of dents on the membrane surface.<sup>38</sup> Following dent formation, the nanosheets have been found to cause extensive extraction of phospholipid molecules from the lipid bilayer thereby destabilizing the membrane structure and integrity.<sup>38</sup> This combined effect of dent formation and subsequent phospholipid extraction is expected to be the main driving force behind the rapid membrane depolarization that we observed in case of CS-MoS<sub>2</sub> nanosheets. It is to be further noted that the presence of a layer of positively charged chitosan molecules on the surface of MoS<sub>2</sub> nanosheets might contribute toward initiating a faster attachment of the nanosheets with the negatively charged bacterial membrane through electrostatic interactions, thereby accelerating the process of membrane depolarization and hence improving its bactericidal efficiency.

**3.3.1.2. Loss of Membrane Integrity.** Next, the effect of the CS-MoS<sub>2</sub> nanosheets on the membrane integrity and bacterial morphology was investigated in detail using fluorescent dye-based assays and SEM to properly elucidate the mechanism of antibacterial action of CS-MoS<sub>2</sub> nanosheets. Five (and 6)-carboxyfluorescein diacetate succinimidyl ester (cFDA-SE) is a

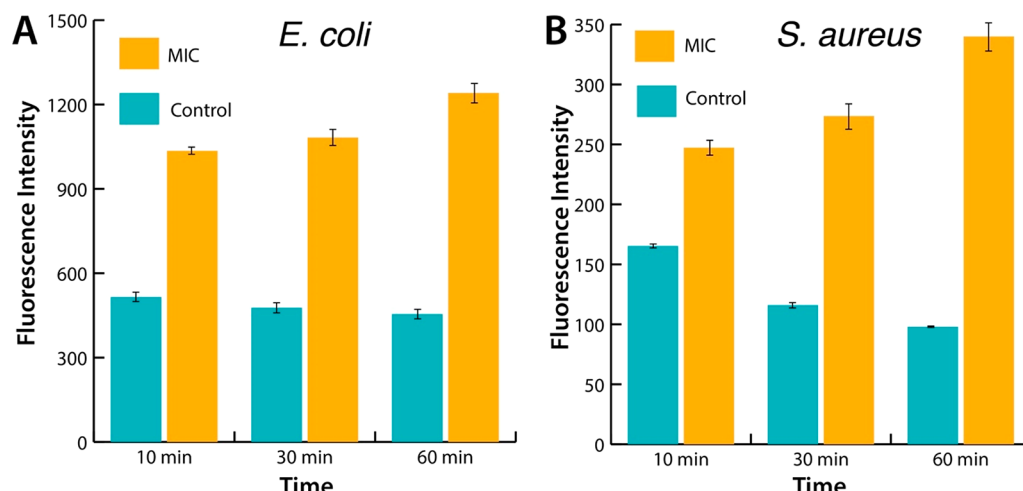


**Figure 5.** Membrane depolarization. Measurement of membrane depolarization using diSC<sub>3</sub>S dye-based fluorescence assay in (A) *E. coli* and (B) *S. aureus* cells treated with CS-MoS<sub>2</sub> nanosheets at their respective MIC values.

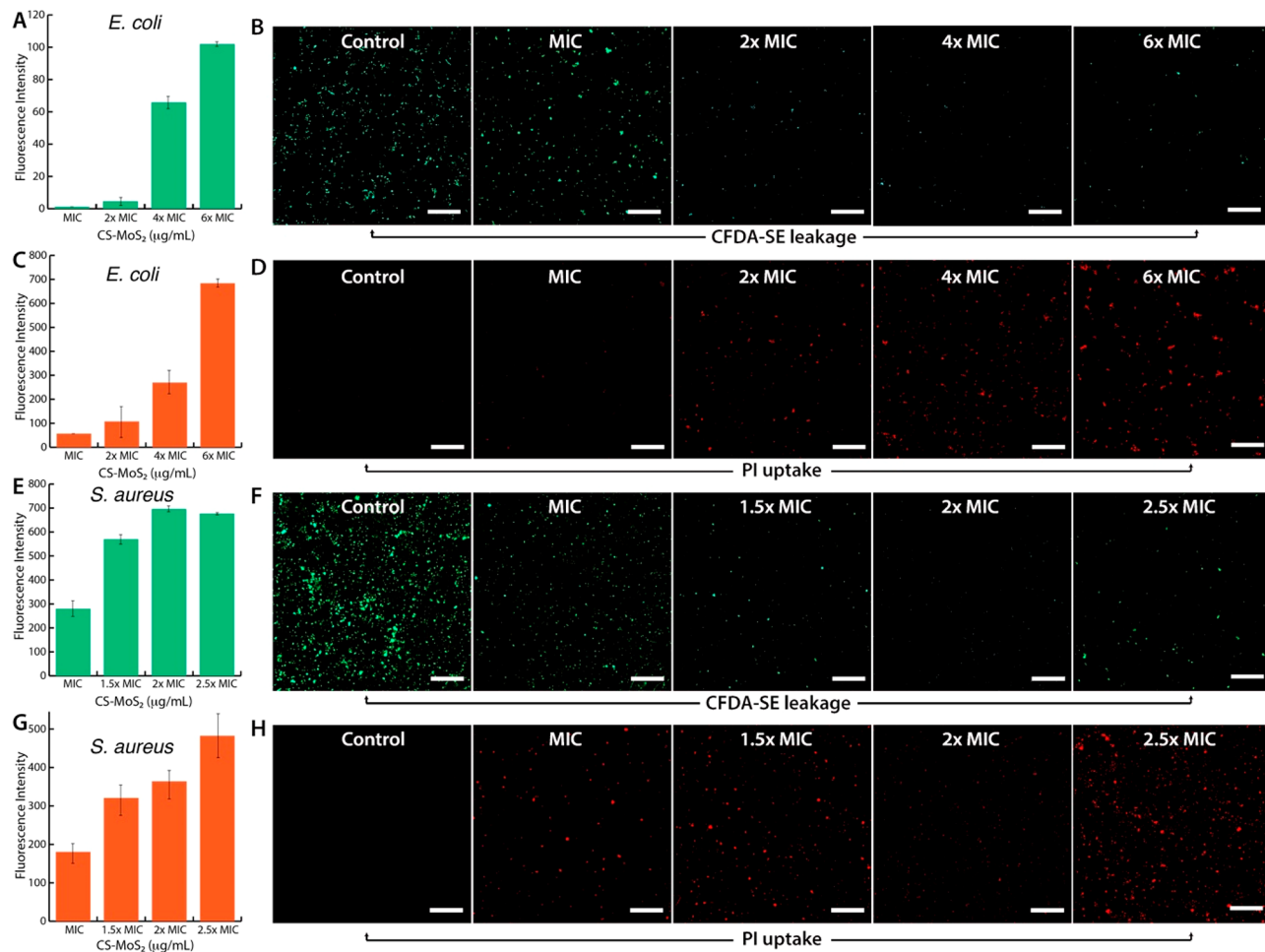


**Figure 6.** Loss of membrane integrity. Estimation of membrane damage using (A, E) cFDA-SE leakage assay and (C, G) PI uptake assay in *E. coli* and *S. aureus* treated with increasing concentrations of CS-MoS<sub>2</sub> nanosheets. Fluorescence micrograph images of CS-MoS<sub>2</sub> nanosheet treated (B, D) *E. coli* and (F, H) *S. aureus* stained with cFDA-SE and PI. Scale bar for all images is 100  $\mu$ m.

membrane permeable dye, which is nonfluorescent in its esterified form. Upon entering cells, the intracellular esterases cleave the ester bond of the dye molecules, thereby converting them into a fluorescent form.<sup>55</sup> Bacterial cells having intact undamaged membranes retain the fluorescent dye molecules and appear green; however, cells with damaged or compromised membranes result in leakage of the dye molecules to the outside leading to an increase in extracellular fluorescence. Leakage of this fluorescent form of the dye from the bacterial cells is used as a direct parameter to study the membrane integrity of the cells. As shown in Figure 6A and E, *E. coli* and *S. aureus* cells stained with cFDA-SE and treated with increasing concentrations of CS-MoS<sub>2</sub> nanosheets demonstrated a dose-dependent increase in the efflux of the dye molecules from the cells as measured from its fluorescence. This clearly showed that the CS-MoS<sub>2</sub> nanosheets upon interacting with the bacterial cells caused extensive membrane damage, which resulted in the leakage of the dye molecules. These results also indicated that the CS-MoS<sub>2</sub> nanosheets were capable of disrupting the membrane integrity of both Gram-positive and negative bacteria, and the extent of this membrane damage increased in a dose-dependent manner. The membrane damaging potential of the nanosheets was further validated by measuring the uptake efficiency of a membrane impermeable dye propidium iodide (PI) by CS-MoS<sub>2</sub> nanosheet treated cells.<sup>56</sup> PI can enter cells only if the

membrane is damaged or compromised. Upon entering cells, PI binds to single and double stranded nucleic acids and produces a strong red fluorescence. The results of the PI uptake assay as depicted in Figure 6C and G further confirmed the potential of CS-MoS<sub>2</sub> nanosheets to cause physical disruption of the lipid bilayer thereby causing cell death. A dose-dependent increase in the PI fluorescence was observed in both *E. coli* and *S. aureus* cells treated with increasing concentrations of CS-MoS<sub>2</sub> nanosheets showing increased uptake of the dye by the membrane compromised cells. Fluorescence microscopy results gave additional support to the occurrence of membrane damage and subsequent loss of viability in cells treated with CS-MoS<sub>2</sub> nanosheets. For both *E. coli* and *S. aureus*, the fluorescence micrographs clearly showed a gradual decrease in the number of cFDA-SE stained green fluorescent cells with increase in nanosheet concentration, which indicated the dose-dependent loss of cell viability (Figure 6B,F). Similarly, a gradual increase in the number of PI stained red fluorescent cells was also observed which further corroborated the results of membrane damage leading to cell death (Figure 6D,H). A concentration of 6  $\times$  MIC for *E. coli* and 2.5  $\times$  MIC for *S. aureus* was found to cause maximum cell death.

SEM analysis of control and treated bacterial cells strongly supported the above results of membrane damage and disruption. The control *E. coli* cells appeared rod-shaped

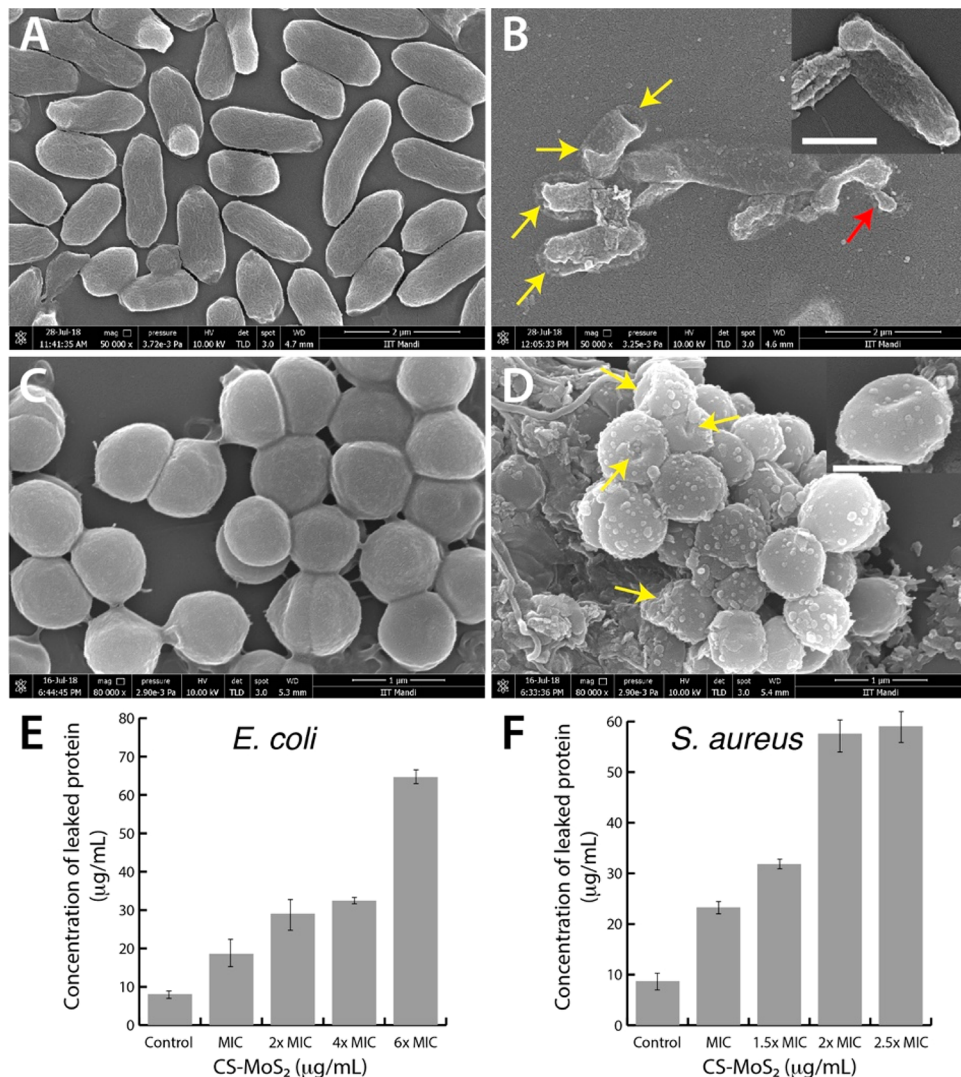


**Figure 7.** SEM analysis of membrane damage and protein leakage. Representative SEM images of (A) untreated and (B) CS-MoS<sub>2</sub> treated *E. coli*. Inset shows the extent of membrane damage. Representative SEM images of (C) untreated and (D) CS-MoS<sub>2</sub> treated *S. aureus*. Inset shows membrane indentation. Scale bars of panels A and B correspond to 2 μm and those of panels C and D correspond to 1 μm. Protein leakage from (E) *E. coli* and (F) *S. aureus* treated with increasing concentrations of CS-MoS<sub>2</sub> nanosheets.

with smooth surface and intact morphology (Figure 7A). However, *E. coli* cells treated with CS-MoS<sub>2</sub> nanosheets showed extensive deformation and membrane rupture (Figures 7B and S6A,B). The surface of the cells appeared rough and crumpled with numerous indentations (yellow arrow) showing the damage caused by the nanosheets. In addition, the rod-shaped morphology of the treated cells was also found to be compromised with the appearance of cellular fragments (red arrows) depicting the extent of structural damage caused by the CS-MoS<sub>2</sub> nanosheets. Similarly, CS-MoS<sub>2</sub> nanosheet treated *S. aureus* cells showed prominent signs of membrane indentation as shown in the inset along with extensive membrane damage and structural deformation (Figure 7D) in comparison to control cells which appeared round and smooth (Figures 7C and S6C,D). CS-MoS<sub>2</sub> nanosheets attached to the surface of the bacterial cells were also clearly visible in the images of the treated cells.

**3.3.1.3. Protein Leakage.** Physical disruption of lipid bilayer is expected to result in the leakage of cytoplasmic contents from bacteria. As a further proof of membrane damage, we next evaluated the leakage of proteins from cells treated with CS-

MoS<sub>2</sub> nanosheets. Figure 7E and F show the results of protein leakage from *E. coli* and *S. aureus*, respectively. It is quite evident from the results that a dose-dependent increase in protein leakage was observed from bacterial cells interacting with CS-MoS<sub>2</sub> nanosheets, which further validated membrane damage and loss of cellular integrity.

Collectively, the results of fluorescence-based assays supported with the data of SEM and protein leakage clearly demonstrate that the antibacterial activity of CS-MoS<sub>2</sub> nanosheets begin with rapid depolarization of the bacterial membrane, which then proceed toward complete disruption of the membrane integrity leading to cell death. It is to be noted that the ability of CS-MoS<sub>2</sub> nanosheets to induce membrane depolarization and cause membrane disruption is a definitive indication of the fact that the synthesized nanosheets are capable of crossing the lipopolysaccharide (LPS) coating in Gram-negative bacteria and the thick peptidoglycan barrier in Gram-positive bacteria to reach the membrane surface. The LPS layer present in Gram-negative bacteria plays a key role in maintaining the permeability barrier across the outer membrane and thus restricts the entry of antimicrobial drugs

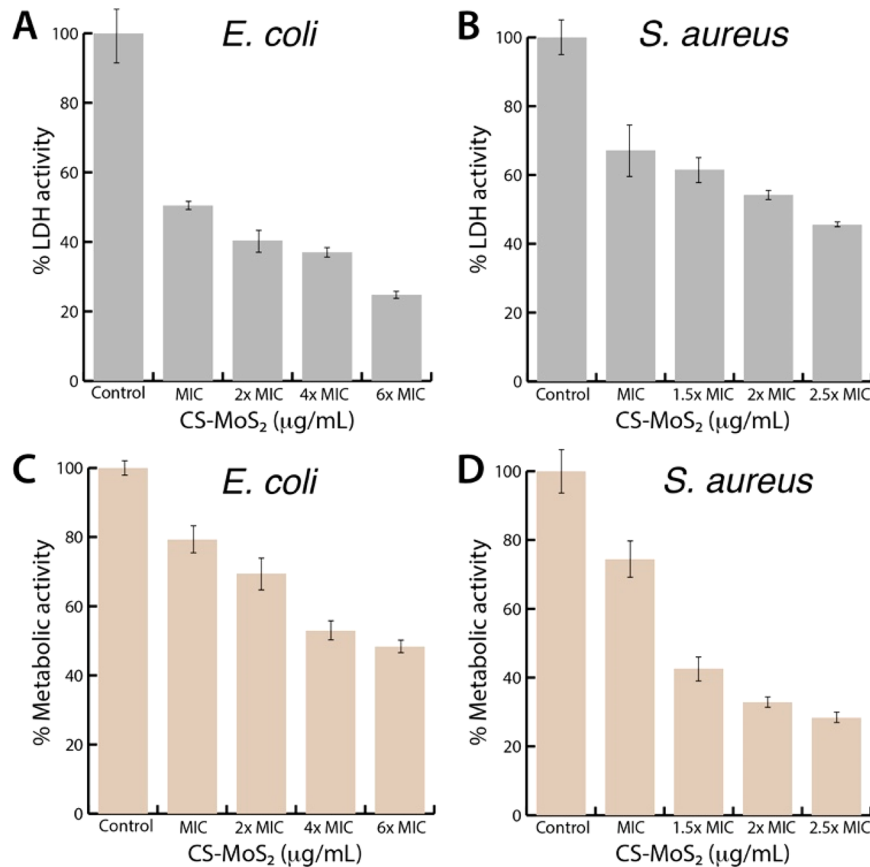


**Figure 8.** LDH inactivation and metabolic arrest. Inactivation of LDH enzyme in (A) *E. coli* and (B) *S. aureus* treated with increasing concentrations of CS-MoS<sub>2</sub> nanosheets. Decrease in metabolic activity of (C) *E. coli* and (D) *S. aureus* treated with increasing concentrations of CS-MoS<sub>2</sub> nanosheets.

and solutes into the cells.<sup>57</sup> Therefore, the potential of CS-MoS<sub>2</sub> nanosheets to overcome this barrier is of great clinical significance especially with respect to treatment of Gram-negative infections.

To gain a better and in-depth understanding of the intracellular events occurring inside bacteria as a consequence of MoS<sub>2</sub> nanosheet interaction and membrane damage, we carried out a set of detailed investigations to decipher the complete mechanism of antibacterial action, the results of which are discussed in the following sections.

**3.3.2. Inhibition of Respiratory Dehydrogenase Activity and Metabolic Arrest.** **3.3.2.1. Inhibition of Lactate Dehydrogenase Activity.** Bacterial respiratory dehydrogenases are a group of membrane bound enzymes that form an integral part of the bacterial respiratory chain and participate in the proper functioning of respiratory metabolism of bacteria.<sup>58</sup> These dehydrogenases belong to the family of oxidoreductases and oxidize a number of organic substrates to generate electrons.<sup>58</sup> These electrons are passed through the electron transport chain for carrying out key metabolic activities such as solute transport and ATP synthesis. One such enzyme present in bacteria is lactate dehydrogenase (LDH), which is known to be a peripheral membrane bound protein attached to the cytoplasmic side of the inner membrane and is key in maintaining the redox balance inside the cells.<sup>59,60</sup> As a result, the effect of CS-MoS<sub>2</sub> nanosheet mediated membrane damage on the biological function of these membrane-bound enzymes was probed by measuring the activity of LDH in treated and control cells. The activity of LDH was measured by monitoring

the ability of bacterial cells to convert a colorless tetrazolium dye into a dark red formazan by the dehydrogenases. The absorbance of the formed formazan was measured at 490 nm and expressed as % LDH activity with respect to control. The results clearly showed that interaction of bacteria with CS-MoS<sub>2</sub> nanosheets greatly affected the activity of LDH. As can be seen in Figure 8A, a 50% decrease in LDH activity was observed in *E. coli* treated with CS-MoS<sub>2</sub> nanosheets at its MIC value. With increase in nanosheet concentration, the activity of LDH was found to further decrease gradually and reach 25% at a concentration of 6 × MIC. Similarly, in the Gram-positive bacterium *S. aureus* (Figure 8B), a concentration-dependent decrease in LDH activity was observed showing the ability of CS-MoS<sub>2</sub> nanosheets to significantly affect the biological activity of respiratory dehydrogenases in both Gram-negative and positive bacteria and thus hamper the respiratory function of the cells. This inhibition of respiratory enzymes observed in our study originate from the extensive membrane damage and disruption caused by the CS-MoS<sub>2</sub> nanosheets. Being membrane bound in nature, the biological activity of these respiratory dehydrogenases greatly depends on the proper orientation of their active sites and their association with the membrane. Physical disruption of the lipid bilayer as observed with CS-MoS<sub>2</sub> nanosheets leads to possible detachment of these proteins from the membrane surfaces, which can further result in loss of structural integrity of the enzymes, ultimately causing their inactivation.

**3.3.2.2. Metabolic Arrest.** The cellular metabolic activity of the bacterial cells undergoing treatment was further evaluated

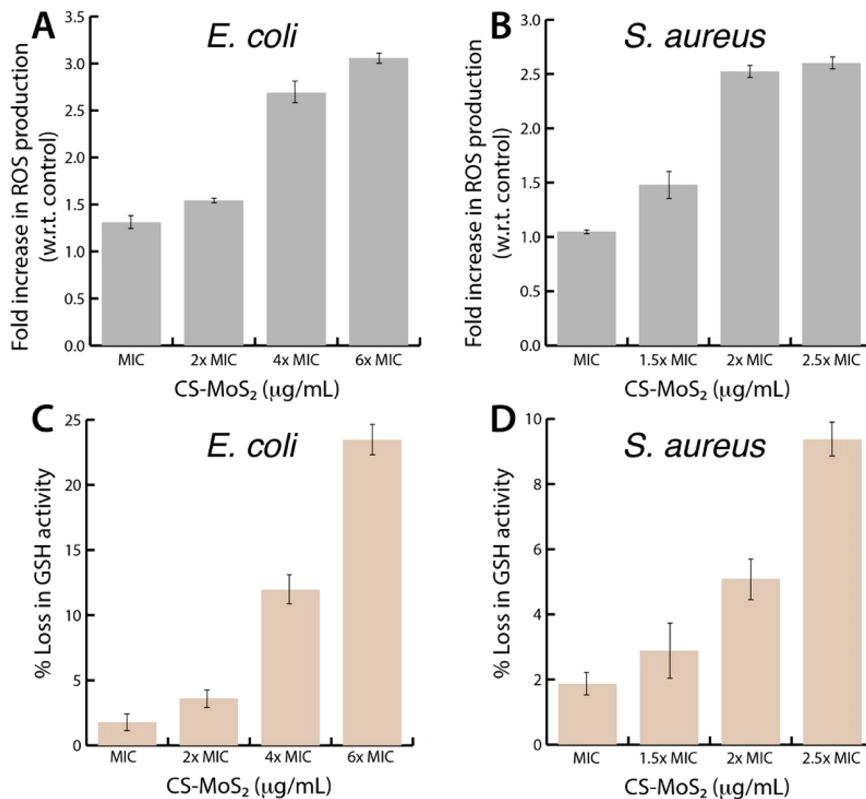


**Figure 9.** Intracellular ROS production and GSH oxidation. Fold increase in ROS production in (A) *E. coli* and (B) *S. aureus* treated with increasing concentrations of CS-MoS<sub>2</sub> nanosheets. % loss in GSH activity in (C) *E. coli* and (D) *S. aureus* treated with increasing concentrations of CS-MoS<sub>2</sub> nanosheets.

using Alamar blue (Resazurin) assay. The assay is based on the ability of cells to convert a purple nonfluorescent dye resazurin to its pink fluorescent reduced form resofurin. This reduction process is catalyzed by functionally active enzymes and thus occurs only in viable or metabolically active cells.<sup>41</sup> Thus, the degree of reduction of resazurin to resofurin acts as an indicator of metabolic activity of cells. The results depicted in Figure 8C and D showed that the metabolic activity of *E. coli* and *S. aureus* cells decreased upon treatment with CS-MoS<sub>2</sub> nanosheets. With increasing concentration of nanosheets, a gradual decline in the metabolic activity of the cells was noticed, which ultimately rendered them metabolically inactive. Thus, the above results clearly established that the loss of membrane integrity of bacterial cells upon interacting with CS-MoS<sub>2</sub> nanosheets significantly hampered the cellular respiration of the cells by inhibiting the respiratory dehydrogenases, which then uncoupled respiration from oxidative phosphorylation causing metabolic arrest and loss in cell viability.

**3.3.3. Intracellular Oxidative Stress and Glutathione Oxidation.** **3.3.3.1. Intracellular ROS Production.** Generation of intracellular oxidative stress in the form of reactive oxygen species (ROS) has been found to significantly contribute toward the antibacterial activity of many nanomaterials through oxidative damage to essential cellular components such as proteins and nucleic acids.<sup>61,62</sup> To check whether CS-MoS<sub>2</sub> nanosheet mediated membrane damage can result in induction of oxidative stress, we measured the levels of intracellular ROS in treated and control cells using DCFH-DA dye based fluorometric assay. In the presence of ROS, the nonfluorescent DCFH-DA dye is oxidized to form a green

fluorescent molecule called dichlorofluorescein (DCF), which acts as the indicator of ROS.<sup>63</sup> It was observed that treatment of both *E. coli* and *S. aureus* cells with CS-MoS<sub>2</sub> nanosheets resulted in significant production of intracellular ROS as depicted in Figure 9A and B. *E. coli* and *S. aureus* cells treated with CS-MoS<sub>2</sub> nanosheets at their respective MIC concentrations showed around 1.3- and 1.05-fold increase in ROS production, respectively, as compared to untreated control cells. The extent of ROS production was found to be highly dependent on the concentration of nanosheets and increased with nanosheet concentration. A three-fold increase in ROS production was observed in *E. coli* treated at 6 × MIC (180  $\mu\text{g/mL}$ ). For *S. aureus*, a 2.7-fold increase was noticed at 2.5 × MIC (225  $\mu\text{g/mL}$ ). This is in good accordance with our observed dose-dependent membrane damage data and shows that with increase in membrane damage more oxidative stress is generated inside the cells leading to enhanced antibacterial activity. In addition to this, we also speculate that the generation of ROS inside the bacterial cells could be attributed to the intrinsic material property of CS-MoS<sub>2</sub> nanosheets themselves. Previous studies have reported that both 1T-MoS<sub>2</sub> and 2H-MoS<sub>2</sub> are capable of generating acellular/abiotic ROS.<sup>21,37</sup> Therefore, owing to the small size of the synthesized nanosheets (~125 nm), it is highly possible that the CS-MoS<sub>2</sub> nanosheets after disrupting the lipid bilayer enter the bacterial cells and contribute toward further generation of ROS in combination with membrane damage induced oxidative stress, thereby improving the overall efficiency of the antibacterial action. It may be mentioned here that preliminary studies on the antibacterial action of CS-MoS<sub>2</sub> nanosheets of varying sizes (mean ~580 nm, ~240 nm, and ~125 nm) on *E. coli* and *S.*

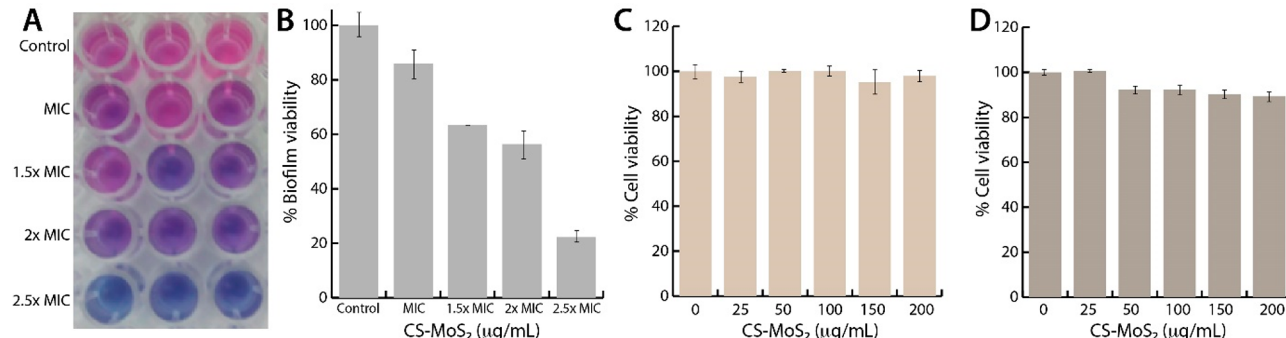


**Figure 10.** Antibiofilm activity and cytotoxicity of CS-MoS<sub>2</sub> nanosheets. (A, B) Effect of CS-MoS<sub>2</sub> nanosheets on the viability of *S. aureus* biofilm. % Cell viability of (C) MCF-7 and (D) HEK-293A cells treated with CS-MoS<sub>2</sub> nanosheets (0–200 μg/mL) for 24 h.

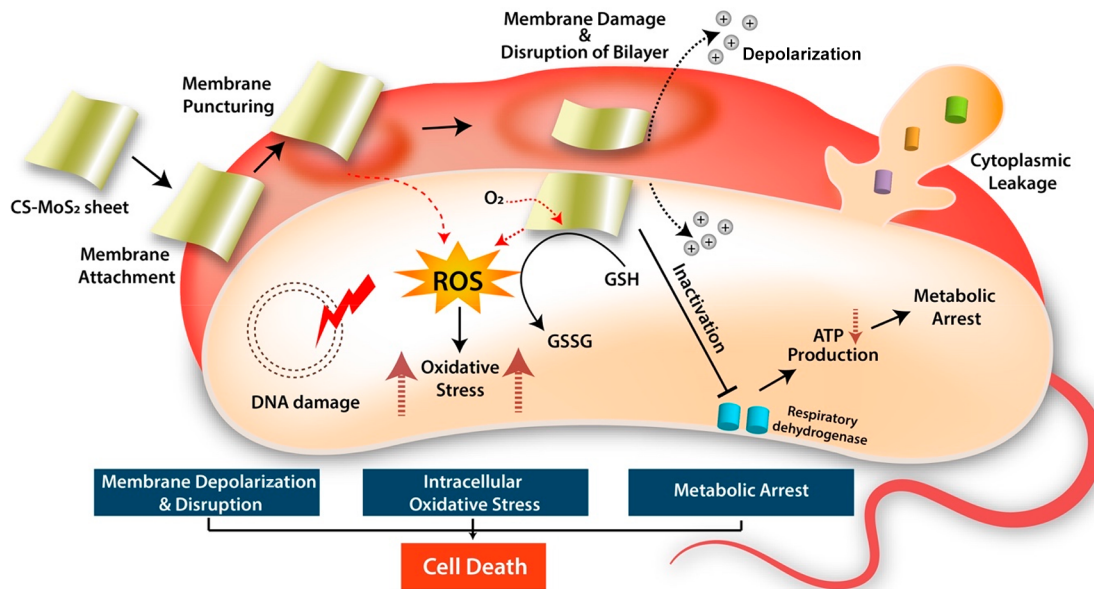
*aureus* indicated a size-dependent antibacterial action with smaller nanosheets showing higher bactericidal efficacy (Figure S7). One possible reason behind this observed size-dependency could be attributed to the presence of high-density defects and dangling bonds at the edges in sheets of smaller size as compared to larger ones, arising from extensive breaking down of sheets during sonication. A high density of surface defects in graphene oxide sheets has been shown to contribute toward more oxidative stress generation with concurrent enhanced antibacterial efficacy.<sup>18</sup> Although such size-dependent antibacterial action of MoS<sub>2</sub> nanosheets indicated the role of ROS in bactericidal response of MoS<sub>2</sub> nanosheets, detailed future investigation is warranted to fully understand the interplay of size-dependent antibacterial efficacy and ROS generation.

**3.3.3.2. Intracellular Glutathione Oxidation.** The effect of the oxidative stress on the normal functioning of bacterial cells was further evaluated by measuring the level of glutathione (GSH) activity in the cells treated with CS-MoS<sub>2</sub> nanosheets. GSH is a thiol containing tripeptide, which is found in high concentrations in its reduced form in both prokaryotes and eukaryotes.<sup>64</sup> It acts as an antioxidant and maintains the cellular redox environment, which helps in protecting cells from oxidative stress induced damage. Production of excessive ROS inside the cells disturbs the equilibrium of the prooxidant–antioxidant system and leads to the oxidation of GSH to GSSG. The oxidized glutathione (GSSG) is unable to protect the cells from the oxidative damage, which further results in oxidation of other essential cellular components such as nucleic acids, proteins, lipids, etc., ultimately leading to cell death. This oxidation of GSH to GSSG resulting in a loss of GSH activity acts as an indicator of intracellular oxidative stress and can be measured quantitatively using Ellman's assay. As shown in Figure 9C, *E. coli* cells treated with increasing concentrations of CS-MoS<sub>2</sub> nanosheets demonstrated a progressive loss in GSH activity, which clearly indicated that the generated ROS was capable of overcoming the antioxidant defense system and caused cellular damage. A similar trend was observed with *S. aureus*, which also showed a gradual decline in GSH activity (Figure 9D). We observed that treatment of *E. coli* and *S. aureus* cells with CS-MoS<sub>2</sub> nanosheets at their respective 6 × MIC and 2.5 × MIC values resulted in 25% and 11% loss in GSH activity, respectively, as compared to control cells. Here, we would also like to highlight the fact that the observed loss in GSH activity can also be contributed by the internalized CS-MoS<sub>2</sub> nanosheets directly in a ROS-independent manner, in addition to ROS-dependent oxidation. Studies have reported the ability of MoS<sub>2</sub> nanosheets to cause acellular

GSH oxidation, thereby implicating their ability to induce a ROS-independent oxidative stress as a mechanism of bactericidal action.<sup>26,37</sup> Therefore, on the basis of the above results and the reported findings, we propose that CS-MoS<sub>2</sub> nanosheets exert their antibacterial action through a combined effect of ROS-dependent and ROS-independent oxidative stress, where the nanosheet induced membrane damage contributes toward the generation of ROS-dependent oxidative stress and the intrinsic material properties of the MoS<sub>2</sub> nanosheets gives rise to the ROS-independent oxidative damage.

#### 3.4. Antibiofilm Activity of CS-MoS<sub>2</sub> Nanosheets.

Growth of biofilms on the surfaces of implants and surgical instruments has been a serious issue of global health concern.<sup>65</sup> Eradication of biofilms using conventional antibiotics has been found to be unsuccessful due to the resistant nature of biofilms toward drugs or antibiotics.<sup>66</sup> The response of biofilms toward conventional antibiotics and drugs has been found to be very different from that of its planktonic counterpart. In biofilms, the bacterial cells are embedded in a secreted extracellular polymeric substance, which protects the cells from the action of antimicrobial agents and antibiotics, thereby making their eradication very difficult.<sup>67</sup> Therefore, there is a dire need for development of agents that can inhibit the growth of biofilms on a surface or can directly kill or eradicate the biofilms. Among the different opportunistic pathogens that are known to form biofilm, *S. aureus* is considered to be a very potent biofilm forming organism and is also a major cause of biofilm-based infections in human.<sup>68</sup> Owing to the membrane-directed antibacterial action of CS-MoS<sub>2</sub> nanosheets as elucidated in this work, we checked the potential of these nanosheets to act as antibiofilm agents. The effect of CS-MoS<sub>2</sub> nanosheets on the viability of *S. aureus* biofilms was investigated using Alamar blue assay by treating the *S. aureus* biofilms with increasing concentrations of CS-MoS<sub>2</sub> nanosheets (Figure 10A,B). Exposure of *S. aureus* biofilms to increasing concentration of CS-MoS<sub>2</sub> nanosheets resulted in a dose-dependent decline in the viability of the biofilm (Figure 10B), clearly establishing the potential of these nanosheets to act as antibiofilm agents. Treatment of the biofilms at 2.5 × MIC concentration resulted in 80% decrease in biofilm viability as compared to untreated biofilms, which showed the highly efficient nature of CS-MoS<sub>2</sub> nanosheets in eradicating the *S. aureus* biofilms. Figure 10A shows the corresponding microplate image of the grown biofilms treated with CS-MoS<sub>2</sub> nanosheets and probed with resazurin dye. The control or untreated wells showed the formation of pink color of resofurin, which indicated the metabolically active or viable state of the biofilms growing in

Scheme 2. Schematic Showing Proposed Mechanism of Antibacterial Action of CS-MoS<sub>2</sub> Nanosheets

those wells. On the other hand, as we increased the concentration of the nanosheets from MIC to  $2.5 \times$  MIC, we observed a gradual disappearance of pink color and appearance of purple or blue color of the resazurin dye, indicating the nonviable state of the treated cells. These results clearly indicate the ability of CS-MoS<sub>2</sub> nanosheets to cross through the extracellular polymeric matrix and gain access to the *S. aureus* cells embedded in the biofilm, thereby causing their membrane damage and death. Thus, the ability of the CS-MoS<sub>2</sub> nanosheets to eradicate biofilm opens up the possibility to further explore this nanomaterial as a surface coating agent for implants and catheters where it can prevent the growth of biofilms on their surface through membrane-directed antibacterial activity.

**3.5. Cytotoxicity of CS-MoS<sub>2</sub> Nanosheets.** Finally, the toxicity of the synthesized CS-MoS<sub>2</sub> nanosheets toward mammalian cells was evaluated to ascertain the therapeutic potential of these nanosheets. Viability of MCF-7 breast cancer cells and HEK-293A normal kidney cells treated with increasing concentrations of CS-MoS<sub>2</sub> nanosheets (25–200  $\mu$ g/mL) was measured using XTT based cell viability assay. The results clearly showed that the nanosheets did not cause any toxicity toward the mammalian cells and were highly biocompatible even at the concentrations that caused complete bacterial death (Figure 10C,D). This showed the highly selective nature of CS-MoS<sub>2</sub> nanosheets to specifically cause toxicity toward the prokaryotic cells in comparison to eukaryotes. The reason for this preferential selectivity can be explained by taking into consideration the membrane structure and composition of bacterial and mammalian cells. Bacterial membranes are mostly composed of phospholipid molecules such as phosphatidylglycerol, cardiolipin, or phosphatidylserine, which impart a net negative charge to the membrane surface.<sup>69</sup> On the other hand, mammalian cells maintain a neutral charge at physiological pH due to the presence of zwitterionic molecules such as cholesterol, sphingomyelin, phosphatidylethanolamine, or phosphatidylcholine in their membrane.<sup>69</sup> The presence of this negatively charged membranes probably results in much stronger interactions of

the cationic nanosheets with the bacterial cells leading to their electrostatic attachment, insertion, and disruption of the bacterial membranes. Such selective cytotoxic behavior toward bacterial cells and biocompatibility toward mammalian cells have also been observed with other antibacterial agents.<sup>70</sup>

**3.6. Proposed Mechanism of Antibacterial Action of CS-MoS<sub>2</sub> Nanosheets.** The mechanism of action of the observed antibacterial activity of CS-MoS<sub>2</sub> nanosheets was found to be a multistep process that started with the attachment of the positively charged MoS<sub>2</sub> nanosheets to the bacterial cell surface via electrostatic interactions, leading to embedding of the nanosheets into the membrane through formation of dents. The strong electrostatic interactions and van der Waals forces between the nanosheets and the phospholipid molecules present in the bacterial membranes pushed the nanosheets further deeper into the membrane, which simultaneously caused extensive extraction of phospholipid molecules by the nanosheets as evidenced by molecular simulations in a different study.<sup>38</sup> This process of nanosheet embedment followed by phospholipid extraction caused the bacterial membranes to undergo rapid depolarization, which altered the permeability across the membrane and triggered the process of membrane disruption. Physical disruption of the lipid bilayer as observed through fluorescence-based assays and SEM resulted in complete loss of membrane integrity and leakage of cytoplasmic contents. Furthermore, the membrane directed antibacterial action of the CS-MoS<sub>2</sub> nanosheets disrupted the bacterial respiratory chain by inhibiting the biological activity of membrane bound respiratory dehydrogenases, which hampered the normal respiratory process in bacteria. Inhibition of respiratory dehydrogenases disconnected respiration from oxidative phosphorylation and resulted in metabolic inactivation of the bacterial cells. In addition to this, significant increase in intracellular oxidative stress in the form of ROS production was also observed as a result of CS-MoS<sub>2</sub> nanosheet interaction and subsequent membrane disruption, which overpowered the antioxidant defense mechanism of bacteria and caused oxidative damage to the cells. Therefore, membrane disruption mediated inactivation of

bacterial respiratory metabolic activity in combination with oxidative damage collectively participated toward the killing of both Gram-negative and Gram-positive bacteria (**Scheme 2**).

#### 4. CONCLUSION

Chitosan exfoliated MoS<sub>2</sub> nanosheets were successfully synthesized by a simple, one-step green process. Electron microscopy of the synthesized nanosheets showed high degree of exfoliation of bulk MoS<sub>2</sub> into monolayered and few-layered nanosheets of uniform size. The nanosheets were also found to be highly stable and well dispersed in aqueous solution. Evaluation of antibacterial activity of the CS-MoS<sub>2</sub> nanosheets revealed the excellent potential of these nanosheets to cause growth inhibition of both Gram-negative and Gram-positive bacteria in a concentration and time-dependent manner. Detailed investigations into elucidating the mechanism of antibacterial action showed that the CS-MoS<sub>2</sub> nanosheets induced bacterial cell death through a combined action of membrane damage, metabolic inactivation, and oxidative stress. The synthesized nanosheets were also found to possess antibiofilm activity and showed high biocompatibility toward mammalian cells. It is of great significance to highlight the fact that the antibacterial and antibiofilm action of the chitosan exfoliated MoS<sub>2</sub> nanosheets were observed without the need for any additional surface functionalization of the nanosheets with complex ligands, biocidal nanoparticles, antimicrobial peptides, photosensitizers, or antibiotics and even in the absence of NIR assisted photothermal action. This property of CS-MoS<sub>2</sub> nanosheets opens up future possibilities for further exploiting them in developing antibacterial coatings, wound dressings, and ultrafiltration membranes for potential biomedical and environmental applications.

#### ■ ASSOCIATED CONTENT

##### Supporting Information

The Supporting Information is available free of charge on the ACS Publications website at DOI: [10.1021/acsabm.9b00124](https://doi.org/10.1021/acsabm.9b00124).

UV-vis spectra of chitosan; FTIR spectra of bulk MoS<sub>2</sub>, chitosan, and CS-MoS<sub>2</sub> nanosheets; XPS survey spectra; high resolution Mo 3d, Mo 3p, S 2p, C 1s, and O 1s spectra of ce-MoS<sub>2</sub>; Mo 3p comparison spectra; SEM of chitosan; size distribution of CS-MoS<sub>2</sub> nanosheets; growth kinetics of *E. coli* and *S. aureus* treated with chitosan and SEM images showing membrane damage in *E. coli* and *S. aureus*; size-dependent antibacterial activity of CS-MoS<sub>2</sub> nanosheets ([PDF](#))

#### ■ AUTHOR INFORMATION

##### Corresponding Authors

\*E-mail: [j.amit@iitmandi.ac.in](mailto:j.amit@iitmandi.ac.in).

\*E-mail: [pallab@dubai.bits-pilani.ac.in](mailto:pallab@dubai.bits-pilani.ac.in).

##### ORCID

Rupantan Banerjee: [0000-0002-5881-1549](https://orcid.org/0000-0002-5881-1549)

Amit Jaiswal: [0000-0002-9748-0404](https://orcid.org/0000-0002-9748-0404)

##### Notes

The authors declare no competing financial interest.

#### ■ ACKNOWLEDGMENTS

A.J. acknowledges the support from BioX Centre and Advanced Materials Research Centre (AMRC), Indian Institute of Technology Mandi for research and infrastructure

facility. S.R. and A.S. would like to acknowledge DST INSPIRE Fellowship programme [IF160513] and MHRD, respectively, for providing doctoral fellowship.

#### ■ REFERENCES

- (1) Levy, S. B.; Marshall, B. Antibacterial resistance worldwide: causes, challenges and responses. *Nat. Med.* **2004**, *10* (12s), S122.
- (2) Brooks, B. D.; Brooks, A. E. Therapeutic strategies to combat antibiotic resistance. *Adv. Drug Delivery Rev.* **2014**, *78*, 14–27.
- (3) Allahverdiyev, A. M.; Kon, K. V.; Abamor, E. S.; Bagirova, M.; Rafailovich, M. Coping with antibiotic resistance: combining nanoparticles with antibiotics and other antimicrobial agents. *Expert Rev. Anti-Infect. Ther.* **2011**, *9* (11), 1035–1052.
- (4) Huh, A. J.; Kwon, Y. J. Nanoantibiotics": a new paradigm for treating infectious diseases using nanomaterials in the antibiotics resistant era. *J. Controlled Release* **2011**, *156* (2), 128–145.
- (5) Dankovich, T. A.; Gray, D. G. Bactericidal paper impregnated with silver nanoparticles for point-of-use water treatment. *Environ. Sci. Technol.* **2011**, *45* (5), 1992–1998.
- (6) Durán, N.; Durán, M.; de Jesus, M. B.; Seabra, A. B.; Fávaro, W. J.; Nakazato, G. Silver nanoparticles: A new view on mechanistic aspects on antimicrobial activity. *Nanomedicine* **2016**, *12* (3), 789–799.
- (7) Jin, C.; Liu, X.; Tan, L.; Cui, Z.; Yang, X.; Zheng, Y.; Yeung, K. W. K.; Chu, P. K.; Wu, S. Ag/AgBr-loaded mesoporous silica for rapid sterilization and promotion of wound healing. *Biomater. Sci.* **2018**, *6* (7), 1735–1744.
- (8) Gallet, S.; Rouanet, J.-M. Silver nanoparticles: their potential toxic effects after oral exposure and underlying mechanisms—a review. *Food Chem. Toxicol.* **2015**, *77*, 58–63.
- (9) Chen, Q.; Zhang, L.; Feng, Y.; Shi, F.; Wang, Y.; Wang, P.; Liu, L. Dual-functional peptide conjugated gold nanorods for the detection and photothermal ablation of pathogenic bacteria. *J. Mater. Chem. B* **2018**, *6* (46), 7643–7651.
- (10) Feng, Y.; Liu, L.; Zhang, J.; Aslan, H.; Dong, M. Photoactive antimicrobial nanomaterials. *J. Mater. Chem. B* **2017**, *5* (44), 8631–8652.
- (11) Zhang, J.; Feng, Y.; Mi, J.; Shen, Y.; Tu, Z.; Liu, L. Photothermal lysis of pathogenic bacteria by platinum nanodots decorated gold nanorods under near infrared irradiation. *J. Hazard. Mater.* **2018**, *342*, 121–130.
- (12) Miao, H.; Teng, Z.; Wang, C.; Chong, H.; Wang, G. Recent Progress in Two-Dimensional Antimicrobial Nanomaterials. *Chem. - Eur. J.* **2019**, *25*, 929.
- (13) Liu, S.; Zeng, T. H.; Hofmann, M.; Burcombe, E.; Wei, J.; Jiang, R.; Kong, J.; Chen, Y. Antibacterial activity of graphite, graphite oxide, graphene oxide, and reduced graphene oxide: membrane and oxidative stress. *ACS Nano* **2011**, *5* (9), 6971–6980.
- (14) Akhavan, O.; Ghaderi, E. Toxicity of graphene and graphene oxide nanowalls against bacteria. *ACS Nano* **2010**, *4* (10), 5731–5736.
- (15) Hu, W.; Peng, C.; Luo, W.; Lv, M.; Li, X.; Li, D.; Huang, Q.; Fan, C. Graphene-based antibacterial paper. *ACS Nano* **2010**, *4* (7), 4317–4323.
- (16) Zhao, J.; Deng, B.; Lv, M.; Li, J.; Zhang, Y.; Jiang, H.; Peng, C.; Li, J.; Shi, J.; Huang, Q.; et al. Graphene oxide-based antibacterial cotton fabrics. *Adv. Healthcare Mater.* **2013**, *2* (9), 1259–1266.
- (17) Feng, Y.; Chen, Q.; Yin, Q.; Pan, G.; Tu, Z.; Liu, L. Reduced Graphene Oxide Functionalized with Gold Nanostar Nanocomposites for Synergistically Killing Bacteria through Intrinsic Antimicrobial Activity and Photothermal Ablation. *ACS Appl. Bio Mater.* **2019**, *2* (2), 747–756.
- (18) Perreault, F.; De Faria, A. F.; Nejati, S.; Elimelech, M. Antimicrobial properties of graphene oxide nanosheets: why size matters. *ACS Nano* **2015**, *9* (7), 7226–7236.
- (19) Agarwal, V.; Chatterjee, K. Recent advances in the field of transition metal dichalcogenides for biomedical applications. *Nano-scale* **2018**, *10* (35), 16365–16397.

- (20) Yadav, V.; Roy, S.; Singh, P.; Khan, Z.; Jaiswal, A. 2D MoS<sub>2</sub>-Based Nanomaterials for Therapeutic, Bioimaging, and Biosensing Applications. *Small* **2019**, *15*, 1803706.
- (21) Liu, C.; Kong, D.; Hsu, P.-C.; Yuan, H.; Lee, H.-W.; Liu, Y.; Wang, H.; Wang, S.; Yan, K.; Lin, D.; et al. Rapid water disinfection using vertically aligned MoS<sub>2</sub> nanofilms and visible light. *Nat. Nanotechnol.* **2016**, *11* (12), 1098.
- (22) Barua, S.; Dutta, H. S.; Gogoi, S.; Devi, R.; Khan, R. Nanostructured MoS<sub>2</sub>-based advanced biosensors: a review. *ACS Appl. Nano Mater.* **2018**, *1* (1), 2–25.
- (23) Devi, R.; Gogoi, S.; Barua, S.; Dutta, H. S.; Bordoloi, M.; Khan, R. Electrochemical detection of monosodium glutamate in foodstuffs based on Au@ MoS<sub>2</sub>/chitosan modified glassy carbon electrode. *Food Chem.* **2019**, *276*, 350–357.
- (24) Gogoi, S.; Khan, R. Fluorescence immunosensor for cardiac troponin T based on Förster resonance energy transfer (FRET) between carbon dot and MoS<sub>2</sub> nano-couple. *Phys. Chem. Chem. Phys.* **2018**, *20* (24), 16501–16509.
- (25) Karunakaran, S.; Pandit, S.; Basu, B.; De, M. Simultaneous Exfoliation and Functionalization of 2H-MoS<sub>2</sub> by Thiolated Surfactants: Applications in Enhanced Antibacterial Activity. *J. Am. Chem. Soc.* **2018**, *140* (39), 12634–12644.
- (26) Pandit, S.; Karunakaran, S.; Boda, S. K.; Basu, B.; De, M. High antibacterial activity of functionalized chemically exfoliated MoS<sub>2</sub>. *ACS Appl. Mater. Interfaces* **2016**, *8* (46), 31567–31573.
- (27) Begum, S.; Pramanik, A.; Gates, K.; Gao, Y.; Ray, P. C. Antimicrobial-Peptide-Conjugated MoS<sub>2</sub> Based Nanoplatform for Multimodal Synergistic Inactivation of Superbugs. *ACS Appl. Bio Mater.* **2019**, *2*, 769.
- (28) Zhang, X.; Zhang, W.; Liu, L.; Yang, M.; Huang, L.; Chen, K.; Wang, R.; Yang, B.; Zhang, D.; Wang, J. Antibiotic-loaded MoS<sub>2</sub> nanosheets to combat bacterial resistance via biofilm inhibition. *Nanotechnology* **2017**, *28* (22), 225101.
- (29) Yin, W.; Yu, J.; Lv, F.; Yan, L.; Zheng, L. R.; Gu, Z.; Zhao, Y. Functionalized nano-MoS<sub>2</sub> with peroxidase catalytic and near-infrared photothermal activities for safe and synergistic wound antibacterial applications. *ACS Nano* **2016**, *10* (12), 11000–11011.
- (30) Feng, Z.; Liu, X.; Tan, L.; Cui, Z.; Yang, X.; Li, Z.; Zheng, Y.; Yeung, K. W. K.; Wu, S. Electrophoretic Deposited Stable Chitosan@MoS<sub>2</sub> Coating with Rapid In Situ Bacteria-Killing Ability under Dual-Light Irradiation. *Small* **2018**, *14* (21), 1704347.
- (31) Gao, Q.; Zhang, X.; Yin, W.; Ma, D.; Xie, C.; Zheng, L.; Dong, X.; Mei, L.; Yu, J.; Wang, C.; et al. Functionalized MoS<sub>2</sub> Nanovehicle with Near-Infrared Laser-Mediated Nitric Oxide Release and Photothermal Activities for Advanced Bacteria-Infected Wound Therapy. *Small* **2018**, *14* (45), 1802290.
- (32) Zhang, W.; Shi, S.; Wang, Y.; Yu, S.; Zhu, W.; Zhang, X.; Zhang, D.; Yang, B.; Wang, X.; Wang, J. Versatile molybdenum disulfide based antibacterial composites for in vitro enhanced sterilization and in vivo focal infection therapy. *Nanoscale* **2016**, *8* (22), 11642–11648.
- (33) Cao, F.; Ju, E.; Zhang, Y.; Wang, Z.; Liu, C.; Li, W.; Huang, Y.; Dong, K.; Ren, J.; Qu, X. An efficient and benign antimicrobial depot based on silver-infused MoS<sub>2</sub>. *ACS Nano* **2017**, *11* (5), 4651–4659.
- (34) Kim, T. I.; Kwon, B.; Yoon, J.; Park, I.-J.; Bang, G. S.; Park, Y.; Seo, Y.-S.; Choi, S.-Y. Antibacterial activities of graphene oxide–molybdenum disulfide nanocomposite films. *ACS Appl. Mater. Interfaces* **2017**, *9* (9), 7908–7917.
- (35) Alimohammadi, F.; Sharifian Gh, M.; Attanayake, N. H.; Thenuwara, A. C.; Gogotsi, Y.; Anasori, B.; Strongin, D. R. Antimicrobial Properties of 2D MnO<sub>2</sub> and MoS<sub>2</sub> Nanomaterials Vertically Aligned on Graphene Materials and Ti<sub>3</sub>C<sub>2</sub>MXene. *Langmuir* **2018**, *34*, 7192.
- (36) Ali, S. R.; Pandit, S.; De, M. 2D-MoS<sub>2</sub>-Based  $\beta$ -Lactamase Inhibitor for Combination Therapy against Drug-Resistant Bacteria. *ACS Appl. Bio Mater.* **2018**, *1* (4), 967–974.
- (37) Yang, X.; Li, J.; Liang, T.; Ma, C.; Zhang, Y.; Chen, H.; Hanagata, N.; Su, H.; Xu, M. Antibacterial activity of two-dimensional MoS<sub>2</sub> sheets. *Nanoscale* **2014**, *6* (17), 10126–10133.
- (38) Wu, R.; Ou, X.; Tian, R.; Zhang, J.; Jin, H.; Dong, M.; Li, J.; Liu, L. Membrane destruction and phospholipid extraction by using two-dimensional MoS<sub>2</sub> nanosheets. *Nanoscale* **2018**, *10* (43), 20162–20170.
- (39) Goswami, S.; Adhikari, M. D.; Kar, C.; Thiagarajan, D.; Das, G.; Ramesh, A. Synthetic amphiphiles as therapeutic antibacterials: lessons on bactericidal efficacy and cytotoxicity and potential application as an adjuvant in antimicrobial chemotherapy. *J. Mater. Chem. B* **2013**, *1* (20), 2612–2623.
- (40) Parandhaman, T.; Das, A.; Ramalingam, B.; Samanta, D.; Sastry, T.; Mandal, A. B.; Das, S. K. Antimicrobial behavior of biosynthesized silica–silver nanocomposite for water disinfection: A mechanistic perspective. *J. Hazard. Mater.* **2015**, *290*, 117–126.
- (41) Rampersad, S. N. Multiple applications of Alamar Blue as an indicator of metabolic function and cellular health in cell viability bioassays. *Sensors* **2012**, *12* (9), 12347–12360.
- (42) Stepanović, S.; Vuković, D.; Hola, V.; Bonaventura, G. D.; Djukić, S.; Ćirković, I.; Ruzicka, F. Quantification of biofilm in microtiter plates: overview of testing conditions and practical recommendations for assessment of biofilm production by staphylococci. *Apmis* **2007**, *115* (8), 891–899.
- (43) Qiao, W.; Yan, S.; He, X.; Song, X.; Li, Z.; Zhang, X.; Zhong, W.; Du, Y. Effects of ultrasonic cavitation intensity on the efficient liquid-exfoliation of MoS<sub>2</sub> nanosheets. *RSC Adv.* **2014**, *4* (92), 50981–50987.
- (44) Nguyen, E. P.; Carey, B. J.; Daeneke, T.; Ou, J. Z.; Latham, K.; Zhiykov, S.; Kalantar-Zadeh, K. Investigation of two-solvent grinding-assisted liquid phase exfoliation of layered MoS<sub>2</sub>. *Chem. Mater.* **2015**, *27* (1), 53–59.
- (45) Zhang, W.; Wang, Y.; Zhang, D.; Yu, S.; Zhu, W.; Wang, J.; Zheng, F.; Wang, S.; Wang, J. A one-step approach to the large-scale synthesis of functionalized MoS<sub>2</sub> nanosheets by ionic liquid assisted grinding. *Nanoscale* **2015**, *7* (22), 10210–10217.
- (46) Yin, W.; Yan, L.; Yu, J.; Tian, G.; Zhou, L.; Zheng, X.; Zhang, X.; Yong, Y.; Li, J.; Gu, Z.; et al. High-throughput synthesis of single-layer MoS<sub>2</sub> nanosheets as a near-infrared photothermal-triggered drug delivery for effective cancer therapy. *ACS Nano* **2014**, *8* (7), 6922–6933.
- (47) Feng, X.; Wang, X.; Xing, W.; Zhou, K.; Song, L.; Hu, Y. Liquid-exfoliated MoS<sub>2</sub> by chitosan and enhanced mechanical and thermal properties of chitosan/MoS<sub>2</sub> composites. *Compos. Sci. Technol.* **2014**, *93*, 76–82.
- (48) Wang, D.; Song, L.; Zhou, K.; Yu, X.; Hu, Y.; Wang, J. Anomalous nano-barrier effects of ultrathin molybdenum disulfide nanosheets for improving the flame retardance of polymer nanocomposites. *J. Mater. Chem. A* **2015**, *3* (27), 14307–14317.
- (49) Ganta, D.; Sinha, S.; Haasch, R. T. 2-D material molybdenum disulfide analyzed by XPS. *Surf. Sci. Spectra* **2014**, *21* (1), 19–27.
- (50) Bang, G. S.; Nam, K. W.; Kim, J. Y.; Shin, J.; Choi, J. W.; Choi, S.-Y. Effective liquid-phase exfoliation and sodium ion battery application of MoS<sub>2</sub> nanosheets. *ACS Appl. Mater. Interfaces* **2014**, *6* (10), 7084–7089.
- (51) Zhou, W.; Hou, D.; Sang, Y.; Yao, S.; Zhou, J.; Li, G.; Li, L.; Liu, H.; Chen, S. MoO<sub>2</sub> nanobelts@ nitrogen self-doped MoS<sub>2</sub> nanosheets as effective electrocatalysts for hydrogen evolution reaction. *J. Mater. Chem. A* **2014**, *2* (29), 11358–11364.
- (52) Nyholm, R.; Martensson, N. Core level binding energies for the elements Zr–Te (Z= 40–52). *J. Phys. C: Solid State Phys.* **1980**, *13* (11), L279.
- (53) Kiem, S.; Schentag, J. J. Relationship of minimal inhibitory concentration and bactericidal activity to efficacy of antibiotics for treatment of ventilator-associated pneumonia. *Seminars in Respiratory and Critical Care Medicine*; Thieme Medical Publishers, Inc., 2006; pp 051–067.
- (54) Adhikari, M. D.; Goswami, S.; Panda, B. R.; Chattopadhyay, A.; Ramesh, A. Membrane-Directed High Bactericidal Activity of (Gold Nanoparticle)–Polythiophene Composite for Niche Applications Against Pathogenic Bacteria. *Adv. Healthcare Mater.* **2013**, *2* (4), 599–606.

- (55) Hoefel, D.; Grooby, W. L.; Monis, P. T.; Andrews, S.; Saint, C. P. A comparative study of carboxyfluorescein diacetate and carboxyfluorescein diacetate succinimidyl ester as indicators of bacterial activity. *J. Microbiol. Methods* **2003**, *52* (3), 379–388.
- (56) Virto, R.; Manas, P.; Alvarez, I.; Condon, S.; Raso, J. Membrane damage and microbial inactivation by chlorine in the absence and presence of a chlorine-demanding substrate. *Appl. Environ. Microbiol.* **2005**, *71* (9), 5022–5028.
- (57) Nikaido, H. Molecular basis of bacterial outer membrane permeability revisited. *Microbiol. Mol. Biol. Rev.* **2003**, *67* (4), 593–656.
- (58) Kerscher, S.; Dröse, S.; Zickermann, V.; Brandt, U. The three families of respiratory NADH dehydrogenases. In *Bioenergetics*; Springer, 2007; pp 185–222.
- (59) Dym, O.; Pratt, E. A.; Ho, C.; Eisenberg, D. The crystal structure of D-lactate dehydrogenase, a peripheral membrane respiratory enzyme. *Proc. Natl. Acad. Sci. U. S. A.* **2000**, *97* (17), 9413–9418.
- (60) Gaspar, P.; Al-Bayati, F. A.; Andrew, P. W.; Neves, A. R.; Yesilkaya, H. Lactate dehydrogenase is the key enzyme for pneumococcal pyruvate metabolism and pneumococcal survival in blood. *Infect. Immun.* **2014**, *82*, 5099.
- (61) Gurunathan, S.; Han, J. W.; Dayem, A. A.; Eppakayala, V.; Kim, J.-H. Oxidative stress-mediated antibacterial activity of graphene oxide and reduced graphene oxide in *Pseudomonas aeruginosa*. *Int. J. Nanomed.* **2012**, *7*, 5901.
- (62) Radzig, M.; Nadtochenko, V.; Koksharova, O.; Kiwi, J.; Lipasova, V.; Khmel, I. Antibacterial effects of silver nanoparticles on gram-negative bacteria: influence on the growth and biofilms formation, mechanisms of action. *Colloids Surf., B* **2013**, *102*, 300–306.
- (63) Aranda, A.; Sequedo, L.; Tolosa, L.; Quintas, G.; Burello, E.; Castell, J.; Gombau, L. Dichloro-dihydro-fluorescein diacetate (DCFH-DA) assay: a quantitative method for oxidative stress assessment of nanoparticle-treated cells. *Toxicol. In Vitro* **2013**, *27* (2), 954–963.
- (64) Fahey, R.; Brown, W.; Adams, W.; Worsham, M. Occurrence of glutathione in bacteria. *J. Bacteriol.* **1978**, *133* (3), 1126–1129.
- (65) Veerachamy, S.; Yarlagadda, T.; Manivasagam, G.; Yarlagadda, P. K. Bacterial adherence and biofilm formation on medical implants: a review. *Proc. Inst. Mech. Eng., Part H* **2014**, *228* (10), 1083–1099.
- (66) Mah, T.-F. C.; O’toole, G. A. Mechanisms of biofilm resistance to antimicrobial agents. *Trends Microbiol.* **2001**, *9* (1), 34–39.
- (67) Flemming, H.-C.; Wingender, J. The biofilm matrix. *Nat. Rev. Microbiol.* **2010**, *8* (9), 623.
- (68) Savage, V. J.; Chopra, I.; O’Neill, A. J. *Staphylococcus aureus* biofilms promote horizontal transfer of antibiotic resistance. *Antimicrob. Agents Chemother.* **2013**, *57* (4), 1968–1970.
- (69) Arouri, A.; Dathe, M.; Blume, A. Peptide induced demixing in PG/PE lipid mixtures: a mechanism for the specificity of antimicrobial peptides towards bacterial membranes? *Biochim. Biophys. Acta, Biomembr.* **2009**, *1788* (3), 650–659.
- (70) Vudumula, U.; Adhikari, M. D.; Ojha, B.; Goswami, S.; Das, G.; Ramesh, A. Tuning the bactericidal repertoire and potency of quinoline-based amphiphiles for enhanced killing of pathogenic bacteria. *RSC Adv.* **2012**, *2* (9), 3864–3871.